Contributions to Mineralogy and Petrology (2020) 175:63
https://doi.org/10.1007/s00410-020-01699-9

ORIGINAL PAPER

U–Pb geochronology of apatite and zircon from the Brent impact structure, Canada: a Late Ordovician Sandbian–Katian boundary event associated with L-Chondrite parent body disruption

Maree McGregor[1,2] · Michael R. Dence[3] · Christopher R. M. McFarlane[2] · John G. Spray[1]

Received: 10 February 2020 / Accepted: 27 May 2020 / Published online: 13 June 2020

Abstract

In situ LA-ICP-MS U–Pb geochronology has been performed on apatite and zircon within thermally recrystallized clast-laden and clast-poor impact melt rocks from the Brent impact structure. A total of 377 laser analyses on 120 impact melt-grown ($n=9$) and impact-recrystallized zircon grains ($n=111$) were obtained, from which a concordia age of 452.8 ± 2.7 Ma (MSWD 0.57, $n=11$), and a weighted average mean $^{206}Pb/^{238}U$ age of 453.2 ± 2.9 Ma (MSWD 0.60) ($n=11$) are calculated. A total of 300 laser analyses from 100 relict apatite grains were obtained, with an unanchored regression through all data yielding a lower intercept age of 453.2 ± 6.0 Ma (MSWD 5.8, $n=300$), that overlaps within error of zircon. $^{207}Pb/^{206}Pb$ ratios obtained from feldspar clasts within clast-laden impact melt retain the same initial Pb composition as the target rocks from which they are derived, while feldspars that crystallized from impact melt have $^{207}Pb/^{206}Pb$ ratios indicative of isotopic re-equilibration between basement lithologies of two different ages. A similar variability in $^{207}Pb/^{206}Pb$ is recorded by apatite. This provides evidence for the involvement of Neoproterozoic Lake Nipissing alkaline suite, as well as Mesoproterozoic Grenville gneisses in the production of impact melt at Brent. Recrystallized apatite grains exhibit enrichments in light rare earth elements (LREEs) along neoblast grain boundaries, indicative of trace element substitution and phase precipitation during impact-induced recrystallization. An age of 452.8 ± 2.7 Ma from zircon and 453.2 ± 6.0 Ma from apatite places the impact event in the Late Ordovician, at or near the Sandbian–Katian boundary, confirming Brent's involvement in the Middle to Late Ordovician crater cluster event—a period of enhanced impactor flux to Earth related to the L-Chondrite parent body disruption.

Keywords Brent impact structure · LA-ICP-MS · U–Pb geochronology · Apatite · Zircon · Impact-induced recrystallization and phase precipitation · L-Chondrite parent body · Late Ordovician

Introduction

The radiometric dating of terrestrial impact structures is critical for understanding the influence of hypervelocity impact events on Earth. However, obtaining precise and accurate ages from shocked and thermally metamorphosed materials is challenging. Due to the absence of coherent impact melt sheets in many impact structures (i.e., due to either erosion or never having been generated), the majority of lithologies available for radiometric studies are impact melt-bearing breccias (e.g., suevites or clast-laden melt rocks). These may lack impact melt-grown phases that are amenable to dating. As such, the most abundant phases available are inherited grains derived from target lithologies that have been incorporated into impactites. These grains are likely to be heavily shocked

Communicated by Daniela Rubatto.

Electronic supplementary material The online version of this article (https://doi.org/10.1007/s00410-020-01699-9) contains supplementary material, which is available to authorized users.

✉ Maree McGregor
mmcgrego@unb.ca

[1] Planetary and Space Science Centre, University of New Brunswick, Fredericton, NB E3B 5A3, Canada

[2] Department of Earth Sciences, University of New Brunswick, Fredericton, NB E3B 5A3, Canada

[3] 2602-38 Metropole Pvt., Ottawa, ON K1Z 1E9, Canada

and thermally metamorphosed, and/or variably reset due to the heterogeneous nature of shock metamorphism and temperatures within the clast-melt volume (Onorato et al. 1978). Consequently, deciphering meaningful ages from these phases is typically complicated by factors such as target composition (i.e., igneous-metamorphic versus sedimentary; McGregor et al. 2020), temperature–time histories, and the presence of metamict domains in pre-impact grains (Kamo et al. 2011; Schmieder et al. 2019; McGregor et al. 2019a), along with the effects of shock and solid-state recrystallization (e.g., zircon: Kamo et al. 1996; Moser et al. 2011; Kenny et al. 2018).

This study focuses on the 3.4 km-diameter Brent impact structure. Brent is relatively well studied and considered an archetype of the simple meteorite crater form on Earth (Dence 2017). Rapid burial and limited post-exhumation erosion have rendered it well preserved and, in the absence of post-impact tectonism, it remains undeformed. Interest in the crater resulted in over 5 km of drill core being obtained in the 1950s and 1960s, making it one of the better characterized simple structures on Earth (Millman et al. 1960; Dence 1964, 1965). Observations and detailed analysis of these drill cores reveal the presence of a suite of well-preserved impactites, including monomict and polymict breccias, impact melt-bearing breccias (e.g., suevites), impact melt dykes/veins, clast-laden impact melt rocks, and a lenticular body of coherent impact melt rock (Dence 1968, 1971; Grieve 1978).

As for many terrestrial impact structures, the formation age of Brent has been elusive. Early biostratigraphic constraints from fossil assemblages within the uppermost, post-impact sedimentary fill were originally interpreted to indicate a minimum impact age of Lower to Middle Ordovician (Millman et al. 1960; Lozej and Beales 1975). However, subsequent work based on the study of chitinizoans and conodonts refined this to a probable impact age equated with the Late Ordovician and upper Black Riveran (Turinian) times (Grahn and Ormö 1995). Whole rock K–Ar ages on melt rocks samples produced mixed plateau ages of 310–365 Ma (Shafiqullah et al. 1968). Whole-rock K–Ar analysis of coarser crystalline samples from the melt zone provided an age of 414 ± 20 Ma (Hartung et al. 1971) (corrected using Steiger and Jäger (1977) decay constants), which was interpreted as a minimum impact age. Both K–Ar results (implying Devonian–Carboniferous formation) are inconsistent with the age of post-impact sedimentary fill (i.e., the impact event cannot be younger than the overlying sedimentary succession). In the case of Brent, pervasive, apparently impact-related K-metasomatism (Currie 1971; Grieve 1978; Hartung et al. 1971) probably compromised the K–Ar isotope systematics, with post-impact argon loss induced by hydrothermal alteration. Since these studies, no further geochronology has been conducted at Brent.

The application of U–Pb geochronology on accessory mineral phases such as zircon, monazite, titanite and apatite are increasingly being found to provide accurate ages for terrestrial impact events (Erickson et al. 2017; Kenny et al. 2018; Papapavlou et al. 2018; McGregor et al. 2020). Here we report results from an in situ Laser Ablation Inductively Coupled Plasma Mass Spectrometry (LA-ICP-MS) U–Pb investigation of zircon and apatite from Brent. This study provides the first U–Pb age for this well-known terrestrial impact structure, as well as providing insight into the U–Pb behaviour of apatite and zircon under the extreme *P–T–t* conditions resulting from hypervelocity impact.

Geological context

Regional setting

The Brent impact structure is a largely covered, bowl-shaped simple crater located within Algonquin Provincial Park, Ontario, approximately 130 km south of the Grenville–Superior structural boundary (46°04′ N; 78°29′ W) (Fig. 1a). Situated within the northwest-trending Ottawa-Bonnechere graben, the structure was formed within a domain of SE-dipping, strongly deformed gneisses of high metamorphic grade containing conspicuous coronitic metagabbro rocks (Bleeker et al. 2011; Dickin and Strong 2019; Fig. 1a, b). The age of Grenvillian gneisses ranges from 1.9 to 1.0 Ga, and while the gneissic protoliths in the vicinity of Brent are Mesoproterozoic (1.48–1.35 Ga), they experienced overprinting metamorphism during the Ottawan Orogeny at 1.09–1.05 Ga (Rivers 2015). The Grenville rocks in this region were locally affected at 600–577 Ma by igneous activity of the Lake Nipissing alkaline province, which occurred syntectonically with formation of the Ottawa-Bonnechere graben (Fig. 1a; Shafiqullah et al. 1968; Kamo et al. 1995; Bleeker et al. 2011). Magmatic phases associated with this igneous activity include the Central Alkalic Intrusions, the mafic Grenville Dyke swarm (590 ± 2 Ma; Kamo et al. 1995), the alkaline (alnöitic) Mattawa dykes (~ 580 Ma; Shafiqullah et al. 1968), and the alkalic-carbonatitic Callander Complex (577 ± 1 Ma; Kamo et al. 1995) (Fig. 1a). Paleozoic outliers of Upper Ordovician carbonate-rich rocks of the St. Lawrence Platform (up to ~ 200 m thick) unconformably overlie the Grenville basement, but are sporadically distributed due to fault offsetting and preferential erosion associated with Ottawa-Bonnechere graben tectonics (Bleeker et al. 2011) (Fig. 1a).

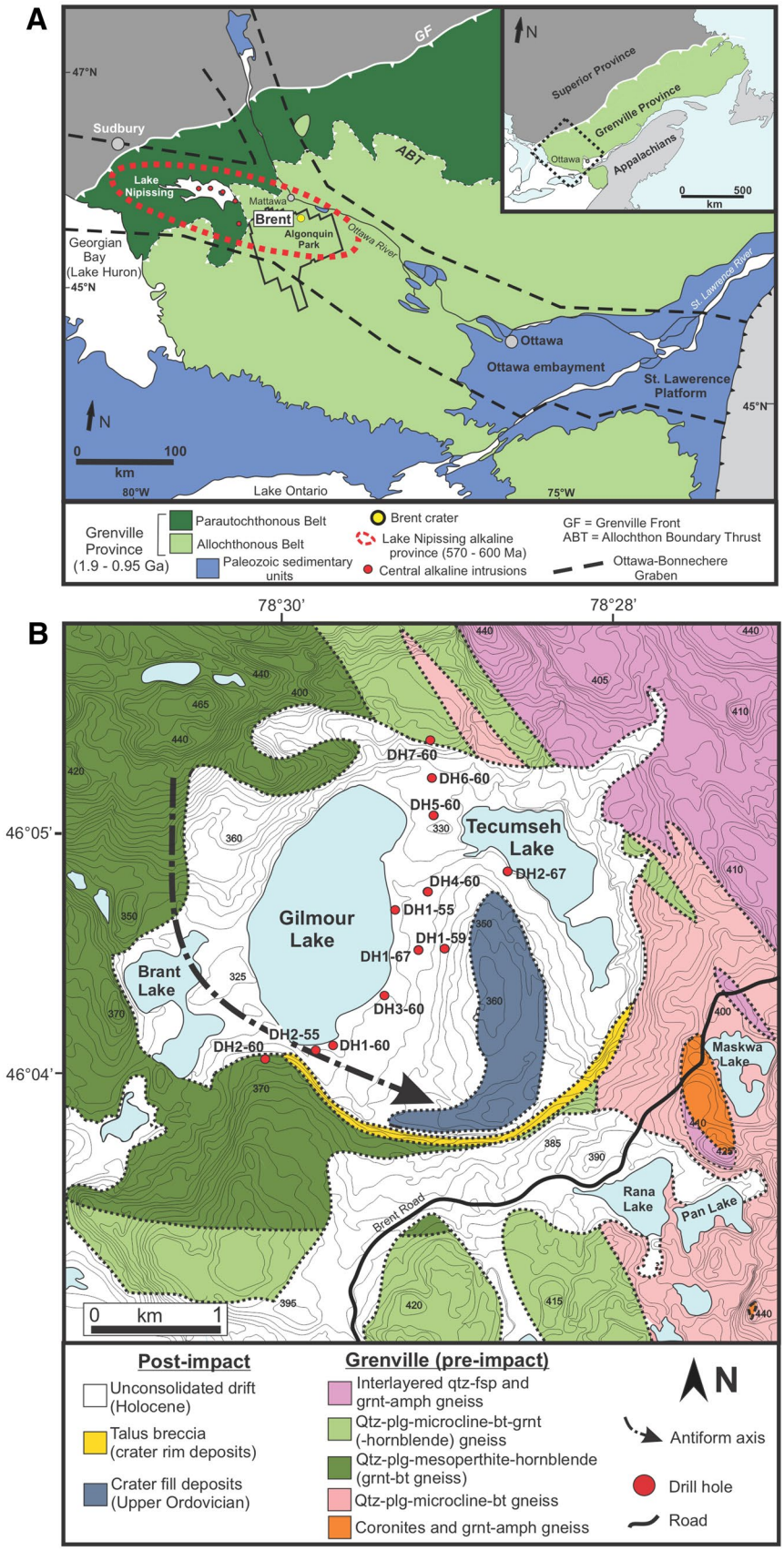

Fig. 1 **a** Simplified regional geology showing the location of the Brent impact structure within the Central Gneiss Belt of the Grenville Province. Modified after Bleeker et al. (2011). **b** Geological map of the Brent impact structure showing location of drill holes. Topographic contours are in 5 m intervals

Crater geology

The Brent impact structure has a roughly circular surficial expression with a diameter of ~ 3.4 km that encompasses two shallow lakes, Gilmour and Tecumseh (Fig. 1b). Topographic, geological and geophysical surveys were first undertaken by the Dominion Observatory (Ottawa, Canada), with extensive diamond drilling conducted between 1955 and 1967, which recovered ~ 5030 m of drill core from 12 holes (Millman et al. 1960; Innes 1964; Dence 1968; Grieve 1978). The crater is mostly obscured by unconsolidated Pleistocene/Holocene drift, but limited surface outcrop and information gathered from drilling indicate that the pre-impact geology at Brent was predominantly Grenvillian acid and basic gneisses, which are locally intruded by alnöitic dykes. The structure lies within the eastern flank of a southeast-plunging antiform, the core of which is composed of mesoperthitic gneiss, which is the dominant basement lithology underlying the crater (Fig. 1b). Microcline-garnet gneisses lie southwest and on the northern flank of the antiform, while microcline-biotite gneisses (containing pods of massive garnet amphibolite and garnet-pyroxene coronites cut by large pegmatites) are situated southeast of the crater (Fig. 1b). East of the antiform, a large SE-dipping synform comprises thinly interlayered granitic and basic garnetiferous gneisses. Although not seen at surface, ultrabasic alnöite dykes of the Lake Nipissing alkaline province are intersected in the drill core. These occur as hypabyssal intrusions within the Grenville basement and as a minor fragments within the aureole breccias, and basal impact melt zone.

Beneath the Pleistocene/Holocene drift (3–40 m in thickness), the crater is infilled by ~ 260 m of undeformed sedimentary rocks (Millman et al. 1960; Lozej and Beales 1975). Given the absence of weathered zones or soil profiles within these units, it has been proposed that sedimentation occurred continuously within 1–2 million years following crater excavation (Lozej and Beales 1975; Grahn and Ormö 1995). Lozej and Beales (1975) recognized ten sedimentary units that are here grouped into five units that distinguish localized (crater-restricted) and regional deposition systems (Fig. 2). The lowermost unit comprises a sequence of sparsely fossiliferous, fine-interbedded siltstones, dolomites, gypsum and calcilutite, consistent with deposition in a restricted saline lake contained within the crater rim (Fig. 2; Lozej and Beales 1975). Overlying this unit is a transgressive sequence of fine, laminated siltstones and sandstones that represent a transition from local (crater-restricted) to regional deposits derived from the encroaching ocean. Regional lithologies overlying these consist of a thin sequence of sandstones and fossiliferous limestones, which are, in turn, overlain by alternating red beds and limestones formed in a salt flat environment (Fig. 2). The uppermost unit, which is preserved at surface in erosion-resistant outcrops at higher elevation (Fig. 2, dashed lines), is massive fossiliferous limestone that reflects regional scale shelf sedimentation in a shallow marine setting (Fig. 2). While drilling indicates that the post-impact Ordovician sequence extends to a depth of ~ 260 m below the crater's centre (Fig. 2; Millman et al. 1960; Currie 1971; Grieve 1978), its preservation below the present height of land requires compaction of both the sedimentary fill and the underlying, originally porous, impactites. It is estimated that the original sequence was ~ 100–150 m thicker than at present, due largely to post-Ordovician accumulation of overlying Silurian and Devonian units that have subsequently been eroded, except in southwest Ontario and New York state. The sedimentary fill of the crater provides important biostratigraphic constraints and a minimum age for the impact event.

Underlying the post-impact sedimentary cover within the crater is a well preserved, ~ 600 m thick sequence of allochthonous impactite lithologies that overlie a fractured and relatively undisturbed crystalline basement (Fig. 2). These comprise an upper zone of polymict breccias interbedded with impact-melt bearing breccias (including suevites), below which lie weakly shocked polymict and monomict breccias that form the bulk of the impactite sequence (Fig. 2). At a depth of approximately 835 m in the central DH1-59 drill core is a lenticular basal melt zone approximately 200 m in radius and 42 m in thickness at its centre (Figs. 2, 3). The central zone of the melt sheet is crystalline and relatively clast-free, and it exhibits an enrichment in chondritic materials (i.e., siderophiles and lithophiles) that preserve an L-Chondrite projectile signature (Grieve 1978; Palme et al. 1981; Goderis et al. 2010). Directly above and below this basal melt zone are clast-laden impact melt rocks that constitute an upper and lower metamorphic aureole (Fig. 3). The breccias above the melt zone are considered collapsed material from the lining of the transient cavity, collectively referred to as "collapse breccias". Those below the melt zone are referred to as "allochthonous breccias", which are derived from fragmented target rocks displaced from below the zone of shock melting (Dence 2017) (Fig. 3). The boundary between the melt zone and the surrounding rocks is transitional, comprising melt-rich veins/dykes, and clast-rich zones formed by the percolation of impact melt between breccia fragments.

Analytical procedures and sample selection

Clast-laden and clast-poor impact melt rocks were selected from the central DH1-59 drill core for U–Pb geochronology (Figs. 2, 3). This core samples the centre of the crater, penetrating Pleistocene/Holocene drift, unmetamorphosed crater-fill sedimentary rocks, impact melt-bearing (suevitic) breccias, a basal melt zone, and clast-laden impact melt rocks within the upper and lower thermal metamorphic aureole

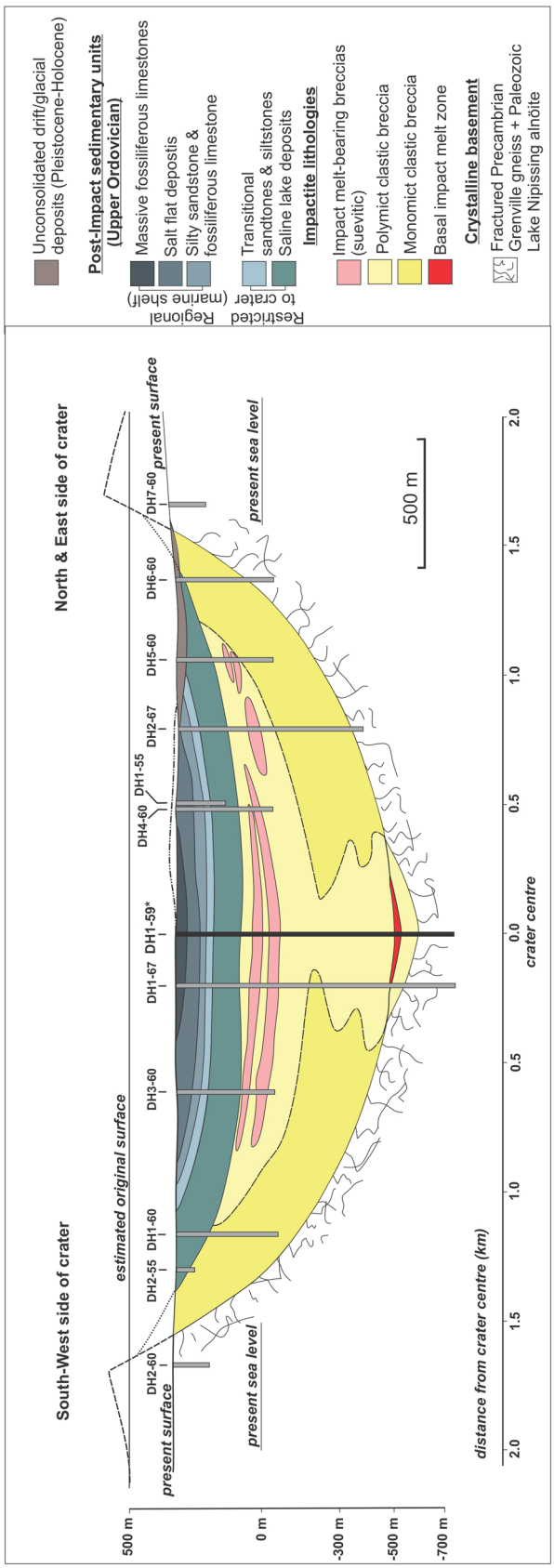

Fig. 2 Cross section profile of the Brent impact structure showing 1) lithologies present, including basement rocks, impactite units and post-impact sedimentary fill units, and 2) drill hole locations highlighting DH1-59 (bold, asterisk; 46° 04.538' N; 78° 28.951' W) used in this study

(Figs. 2, 3). Three groups of samples (eight total) from the DH1-59 drill core were collected for U–Pb geochronology: (a) clast-laden impact melt from the upper thermal aureole (depth: ~ 825–840 m; $n = 3$); (b) clast-poor, crystalline impact melt rock from the centre of the basal melt zone (depth: ~ 845–850 m; $n = 3$), and (c) clast-laden impact melt from the lower thermal aureole (depth: ~ 861–870 m; $n = 2$) (Fig. 3; Table S1).

Polished thin sections were assessed via petrographic microscope and selected based on the quantity of impact melt, and the presence of dateable U-bearing accessory phases. The most abundant phases suitable for U–Pb dating are apatite and zircon, which are newly crystallized from impact melt (igneous) (Fig. 5), or inherited from the underlying target rocks (Figs. 6, 7). Both mineral phases occur as inherited (relict) mineral clasts in these lithologies, while only impact melt-grown zircons were large enough for U–Pb dating (Fig. 5a, b). Individual apatite and zircon grains were selected based on their petrographic setting (inclusions in lithic clasts; mineral clasts in melt matrix), grain size (apatite > 33 µm; zircon > 17 µm) and observed shock-thermal microstructures.

Following optical microscopy, grains selected for U–Pb dating were assessed using backscattered electron (BSE) imaging on a Hitachi SU-70 field emission scanning electron microscope (FESEM) equipped with a Schottky emitter at the University of New Brunswick. Imaging was performed at working distances of 8–10 mm. Mineral phases were analyzed via energy dispersive spectrometry (EDS) at a working distance of 15 mm using an Oxford Instruments INCA X-Act LN_2-free Analytical Silicon Drift Detector with a 20 kV accelerating voltage and a ~ 3 nA beam current. Detection limits are equal to, or better than, 0.1 wt% for major elements.

Micro-X-Ray fluorescence (μ-XRF) was performed on all thin sections at the University of New Brunswick. Data was obtained using a Bruker M4 Tornado micro-XRF spectrometer equipped with a Rh X-ray tube, with analyses obtained at 50 kV and 400 µA under a 20 millibar vacuum and a 20 µm pixel size. Multiphase compositional maps of Ca + P (representing apatite) and Zr (representing zircon) were acquired to highlight the petrographic setting, spatial distribution and relative abundance of each mineral grain. Compositional maps for all thin sections were then imported into the laser ablation software (Geostar v7) and, along with BSE images, served as base maps to guide the selection of apatite and zircon grains during in situ U–Pb geochronology.

A total of 120 zircon grains ($n = 377$ analyses) and 100 apatite grains ($n = 300$ analyses) were selected for in situ U–Pb geochronology. Analyses were conducted at the University of New Brunswick using an Australian Scientific Instruments M-50 193 nm excimer laser ablation system (Complex Pro 110) with a 20 ns pulse width. The ablation system is equipped with a Laurin Technic Pty S-155 two-volume ablation cell coupled to an Agilent 7700 × quadrupole ICP-MS via nylon tubing, and is equipped with dual external rotary pumps. Ablated material was transported to the ICP-MS using a mixed He (300 mL/min) and Ar (930 mL/min) carrier gas. Sensitivity was enhanced using a second external rotary pump and adding N_2 (2.0 mL/min) downstream of the cell. Due to isobaric interference of ^{204}Pb with ^{204}Hg impurities within the carrier gas, direct measurement of the ^{204}Pb signal was permitted using in-line high-capacity Vici Metronics Hg traps within all gas lines entering the cell, ensuring that ^{204}Hg remains < 150 cps under maximum sensitivity conditions. Correction of the ^{204}Hg interference on ^{204}Pb was then performed via peak-stripping using the measured ^{202}Hg on the gas background and assuming a canonical value for ^{202}Hg/^{204}Hg.

Analyses of all unknowns were bracketed with at least 16 spots on primary reference material to monitor and correct for instrument drift, and time-dependent down-hole

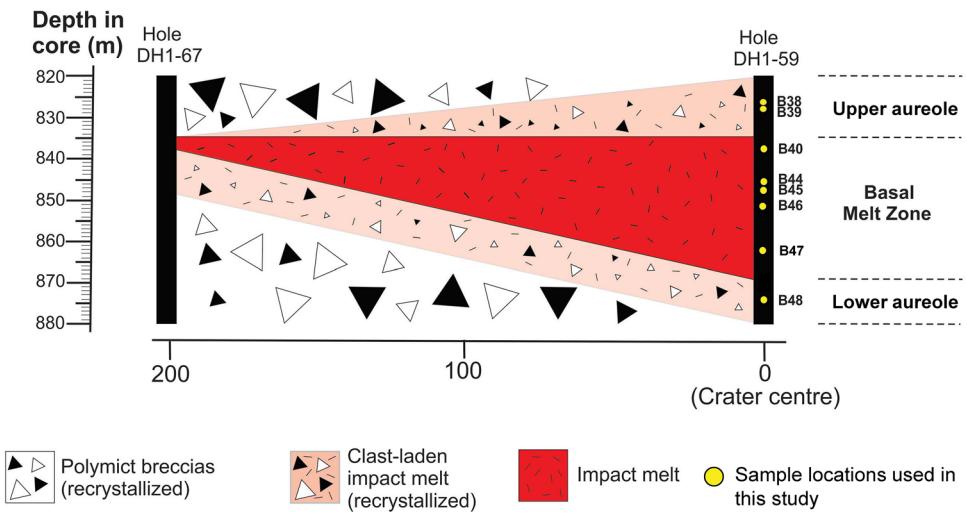

Fig. 3 Simplified diagram showing the nature of basal melt zone and surrounding lithologies as indicated by the DH1-67 and DH1-59 drill cores. The zone is subdivided into the upper and lower aureole units composed of recrystallized clast-laden impact melt rocks, which surround a ~ 30 m thick crystalline melt zone. Modified after Dence (2017). Location of samples used in this study are indicated by yellow circles

fractionation. Drift was modeled using the Iolite3.7™ automatic fit function, whereas down-hole fractionation was modeled using the automatic exponential fit option. The net ^{204}Pb (cps) signal was used for common Pb corrections (if required; see below) for zircon and incorporated into the VizualAge U–Pb data reduction scheme (DRS) (Petrus & Kamber 2012) operating under Iolite3.7™. The routine uses an age estimate based on the measured $^{206}Pb/^{238}U$ and common Pb ratios derived from the evolution curves of Kramers and Tolstikhin (1997). Common Pb corrections were only applied to zircon analyses with net $^{204}Pb > 50$ cps and 1σ internal errors < 30%. All other data remained uncorrected.

Apatite grains were ablated using a laser energy of 4.5 J/cm^3, a repetition rate of 5 Hz, which yielded an ~ 33μm crater diameter. Standards were evenly distributed among the unknowns, with Madagascar (MAD) apatite used as the primary standard (473.5 ± 0.7 Ma; Thomson et al. 2012) and a well characterized inhouse apatite standard from the Laramie Anorthosite Complex (LAC) deployed as the secondary standard (1434.8 ± 7.8 Ma; Scoates and Chamberlain 2003). All zircon grains were analyzed using a laser energy of 3 J/cm^3, a 4 Hz repetition rate, and a 17 µm crater diameter. The primary standard was FC-1 (1098.8 ± 3.4 Ma; Paces and Miller 1993), while Plešovice was used as the secondary standard (333.5 ± 2.2 Ma; Sláma et al. 2008). Additional information on the long-term reproducibility of the secondary standards used are provided in the Supplementary materials. All raw LA-ICP-MS data from each phase was processed off-line using the IgorPro based Iolite3.7™ software (Paton et al. 2011; Petrus and Kamber 2012; Horstwood 2008). Zircon data was processed using the VizualAge DRS (Petrus and Kramer 2012). Due to high and variable common Pb, a modified version of the VizualAge DRS, VizualAge_UcomPbine was used for apatite, where a ^{207}Pb correction is applied to the primary MAD standard (Chew et al. 2014). All apatite age calculations use analyses uncorrected for common Pb. Concentrations for both phases were calculated relative to NIST610 using the Iolite3.7™ trace-element "internal standardization" DRS. All uncertainties quoted in the text, tables and figures are at 2σ, and all ages are reported at the 95% confidence interval.

Lastly, $^{207}Pb/^{206}Pb$ isotopes were obtained from feldspar grains from both crystalline impact melt rock samples (igneous) and feldspar clasts within clast-laden impact melts (inherited metamorphic). Reproducibly was assessed using an inhouse, well-characterized (via Thermal Ionization Mass Spectrometry) feldspar from the Cameron pegmatite (southern Quebec) as the secondary standard, while NIST612 was used as the primary standard. Feldspar grains were ablated at a laser fluence of 5 J/cm^2, a repetition rate of 5 Hz, and 30 s background, which resulted in ~ 112 µm diameter craters.

Impactite petrography

Zircon and apatite grains were evaluated from clast-laden impact melt rocks (recrystallized, contact metamorphic texture) of the upper ($n = 3$) and lower aureole ($n = 2$), and clast-poor, crystalline (igneous textured) impact melt rocks ($n = 3$) from the DH1-59 drill core. (Figs. 3, 4; Table S1). The main mass of impact melt is crystalline and clast-poor to clast-free, with rare mineral and lithic clasts present (< 5%) (Fig. 4c; Table S1). The dominant mineralogy is alkali feldspar with sanidine rims, pyroxene, amphibole and interstitial mica and quartz (Grieve 1978), with the coarsest texture developed in the centre of the melt sheet (i.e., sample B45; Table S1).

The upper and lower aureoles are clast-laden impact melt rocks that are characterized by hornfels (thermally recrystallized) textures. There is a difference in the level of thermal recrystallization between the upper and lower breccias, as indicated by PDFs in quartz, and the presence of ZrO_2 in granular zircon grains. PDFs in quartz from the upper aureole are retained and ZrO_2 within thermally dissociated zircons is preserved, while PDFs are more commonly annealed in the lower aureole, and ZrO_2 has recombined to form neoblastic zircon. Both the upper and lower aureole breccias are composed of variably shocked and altered gneissic (lithic), alnöitic (lithic), and related mineral clasts set within a fine-grained crystalline melt matrix (e.g., Fig. 4a, b). Lithic clast content is 20–80% relative to the melt matrix, with clasts partially digested and variably recrystallized (Fig. 4). Mineral clasts include ilmenite, quartz, biotite, pyroxene, feldspar, apatite and zircon. In samples with > 70% melt matrix, euhedral acicular/hexagonal, REE-rich fluorapatite and crystalline square/prismatic zircons are common accessory phases (Fig. 5). Some zircon grains exhibit possible minor metamict domains (Fig. 5b), and/or display faint magmatic zonation (Fig. 5b). Inherited apatite grains are a mixture of fluorapatite and REE-fluorapatite, while impact melt-grown apatites are all REE-fluorapatite (Table S2). Both impact melt-grown and inherited, REE-fluorapatites (Figs. 5c, d, 7) contain Ce_2O_3, Nd_2O_3, La_2O_3, Y_2O_3 and SiO_2, along with trace amounts of FeO, Na_2O, K_2O, MgO, SrO and Sc_2O_3 (Table S2). While newly grown zircons are devoid of detectable minor components, inherited grains contain trace amounts of ThO_2, HfO_2 and Al_2O_3, with the latter associated with interstitial impact melt at triple junctions (Table S2).

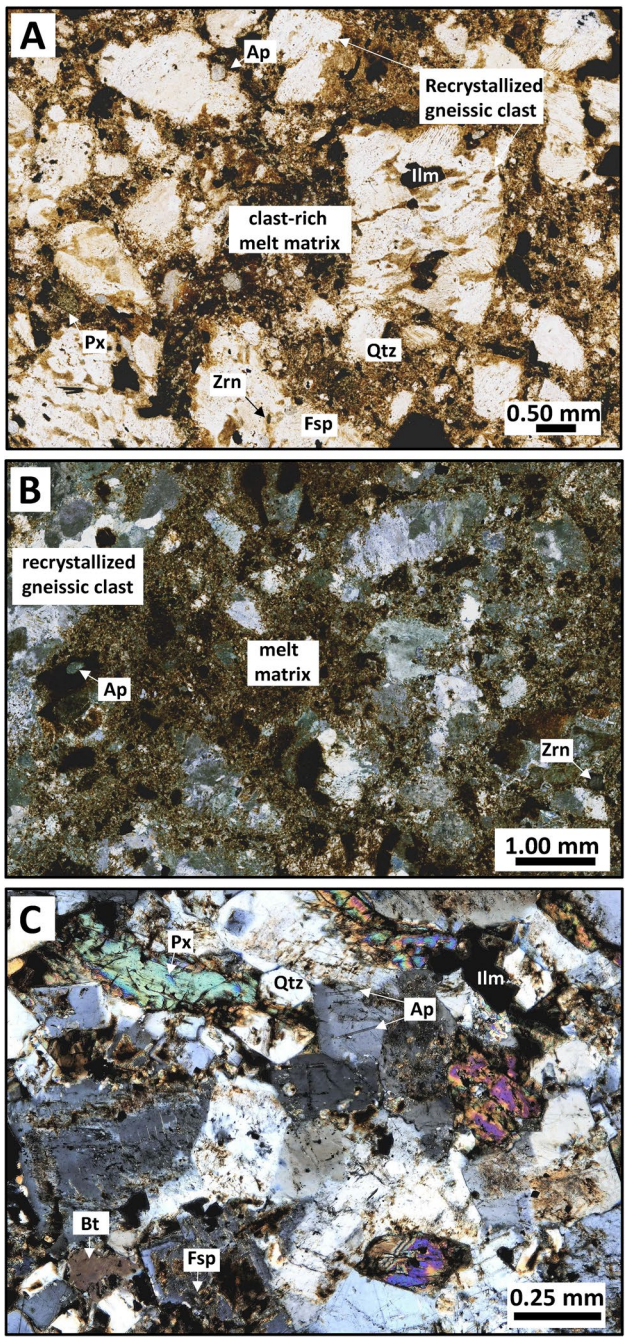

Fig. 4 Optical micrographs of representative lithologies from the DH1-59 drill core used in this study. **a** Thermally recrystallized clast-rich impact melt breccia (i.e., aureole breccia) containing lithic clasts of recrystallized gneiss (Qtz, Fsp, Ilm, Px, Ap, Zrn) situated within a finer grained, clast-rich melt matrix. **b** Thermally recrystallized, clast-poor impact melt breccia containing gneissic lithic clasts situated within a medium-fine grained melt matrix. **c** Course-grained impact melt rock containing interlocking grains of pyroxene, quartz, ilmenite and K-feldspar with altered albite. Biotite occurs as a minor interstitial phase. Elongate apatite occurs as inclusions in feldspar

Shock and thermal microstructures in apatite and zircon

Zircon

All inherited zircon grains have experienced impact-induced recrystallization (i.e., are completely granular; Fig. 6). While EBSD analysis may reveal the presence of important shock features, the BSE images here provide no evidence of microstructures indicative of initial shock pressures (e.g., planar fractures, twins), nor are any pre-impact textures such as metamict domains observed. Several morphological forms of zircon typically occur within a single recrystallized grain, including: (1) 1–2 µm diameter, rounded to sub-rounded neoblasts (Fig. 6a); (2) 1–2 µm diameter prismatic, square, and elongate microcrystals (Fig. 6a, b); and (3) larger (5–30 µm length) prismatic crystals with well-defined grain boundaries (Fig. 6b). The larger zircon crystals occur within individual grains along with sub-micron neoblasts (Fig. 6b), or are developed along grain rims (e.g., Fig. 6c). In addition, granular zircons vary in the degree of impingement (i.e., merging) between individual neoblasts/microcrystals. Regions where neoblasts are merging/impinging exhibit a distinct porous texture, with individual neoblasts not readily discernable (e.g., Fig. 6a, d). In contrast, non-merging neoblasts have well-defined grain boundaries and are surrounded by impact melt (e.g., Fig. 6a, d). In grains where a porous texture is present at a grain's surface, parts of the grain rim are oriented in such a way that some depth is visible, indicating that the entire grain is granular (Fig. 6e). This observation indicates that the porous texture probably reflects triple junctions between sub-micron neoblasts that contain minor amounts of interstitial melt. The presence of ZrO_2 within granular zircon provides evidence of the thermal dissociation of zircon at temperatures > 1673 °C (Wittmann et al. 2006; Timms et al. 2017). This is only observed in grains within the upper aureole. Combined with the preservation of PDFs in quartz within the same samples, this suggests that the upper aureole cooled faster relative to the lower aureole, possibly due to being juxtaposed with cooler overlying collapse breccias.

Apatite

Apatite grains exhibit planar fractures, micro-vesicles, and recrystallization textures (partial and complete), with multiple microstructures co-existing within a single grain (Fig. 7). Planar fractures occur as two or more intersecting sets, are variably annealed, and may co-exist with micro-vesicles, and neoblasts/crystallites (Fig. 7a). Grains

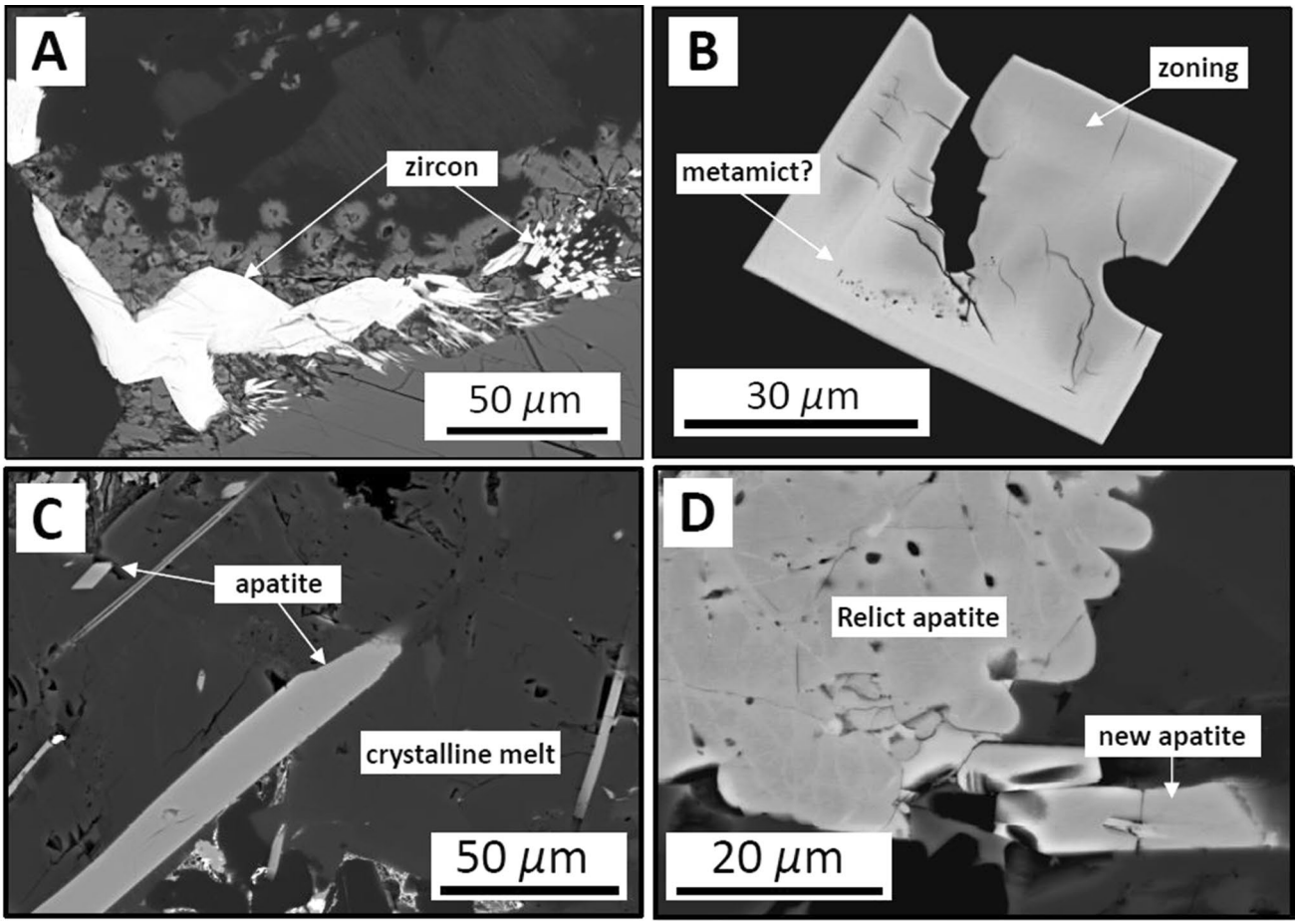

Fig. 5 BSE images of impact melt grown (igneous) apatite and zircon within melt rich clast-laden melt rocks and the basal impact melt zone. **a** Large melt-grown zircon grain with smaller, acicular crystals nucleating off rim. **b** Smaller zircon grain with a square habit showing faint magmatic zoning and possible metamict domain. **c** Acicular apatite crystals within crystalline melt. **d** New apatite nucleated on recrystallized relict apatite grain

are typically cataclastically deformed and composed of individual angular fragments that follow the approximate orientation of planar fractures. Smaller fragments within the same grain are commonly recrystallized, with small (< 5 μm) sub-rounded neoblasts dispersed between larger fragments (Fig. 7a).

All analyzed apatites contain micro-vesicles, although their abundance and texture vary within, and between, individual grains. Grains with the highest densities of micro-vesicles occur as mineral clasts within the melt matrix of clast-laden impact melts, or within clast-poor crystalline impact melt rocks. Strongly vesiculated grains typically manifest evidence of recrystallization (exhibiting triple junctions and neoblasts; Fig. 7b, c). Micro-vesicles occur with two distinct morphologies: (1) rounded to sub-rounded; either randomly distributed or forming linear to sublinear trails that exhibit a degree of curvature (e.g., Fig. 7a–c), or (2) elongate, and oriented parallel to the c axis of the host grain, suggesting the former presence of monazite within the host apatite (Harlov et al. 2002) (Fig. 7b). EDS element mapping indicates that micro-vesicles are either Al-rich (Fig. S1) or infilled by a high-density (bright), REE-rich phase (Fig. S2).

Partly recrystallized apatites are common in clast-laden melt rocks, and are defined by the local presence of neoblasts (rounded to sub-rounded) (e.g., Fig. 7a) or crystallites (euhedral, prismatic or hexagonal) nucleated along host grain rims (e.g., Fig. 7c; Fig. 5d). In contrast, apatites within clast-poor impact melt rocks are more completely recrystallized, with neoblasts and euhedral crystallites distributed throughout entire grains that exhibit well-defined grain boundaries and triple junctions (Fig. 7b–f). In some apatites, the grain interior is composed of semi-isolated neoblasts with rims of euhedral crystallites that have separated from the host grain (Fig. 7e). In certain grains, EDS mapping indicates that the areas surrounding apatite neoblasts comprise Al, Si, and Fe (Fig. S1), which is probably altered impact melt/glass.

A striking feature of recrystallized apatite grains observed at Brent is the presence of LREE enrichments along neoblast

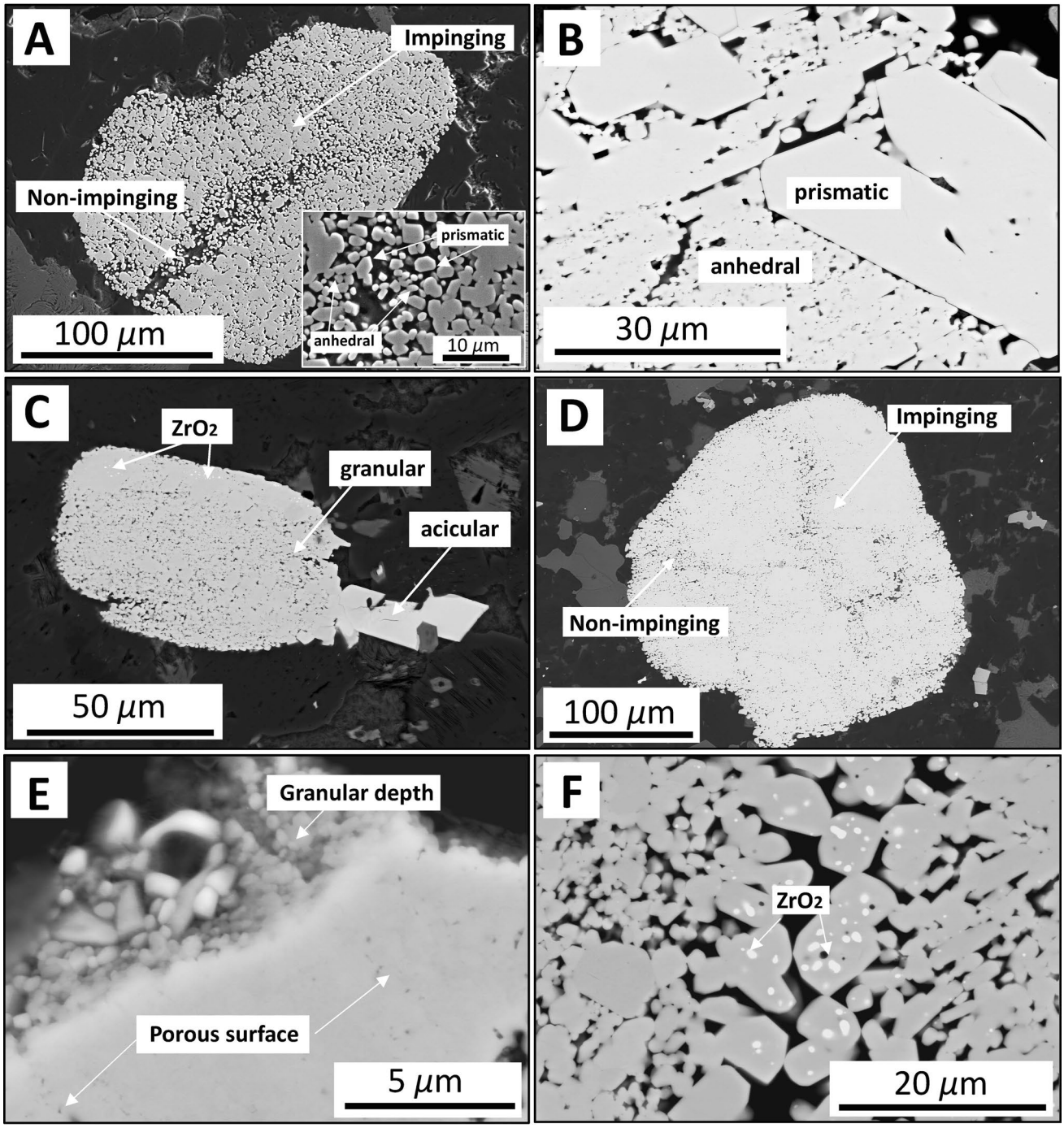

Fig. 6 Representative BSE images of shock recrystallization textures observed in zircon. All grains are completely recrystallized (i.e., granular) in the upper and lower aureole breccias and within impact melt samples. **a** Zircon composed of both anhedral, rounded to sub-rounded neoblasts and square/prismatic euhedral crystals. Variation in the degree of neoblast/crystal "impingement" throughout the grain. **b** Recrystallized grain contains both sub-micron, anhedral grains and neoblasts with variable degrees of impingement, and larger (10–30 μm) prismatic crystals. **c** Granular zircon with large, euhedral zircon crystal nucleated along grain rim. **d** Recrystallized grain with both "impinging" and "non-impinging" domains. **e** Rim of zircon grain with a porous/impinging surface showing the depth into the granular interior along the rim. **f** Granular zircon from upper breccia unit containing neoblasts of variable morphologies (rounded/sub-rounded, euhedral prismatic and square). Note inclusions of ZrO_2

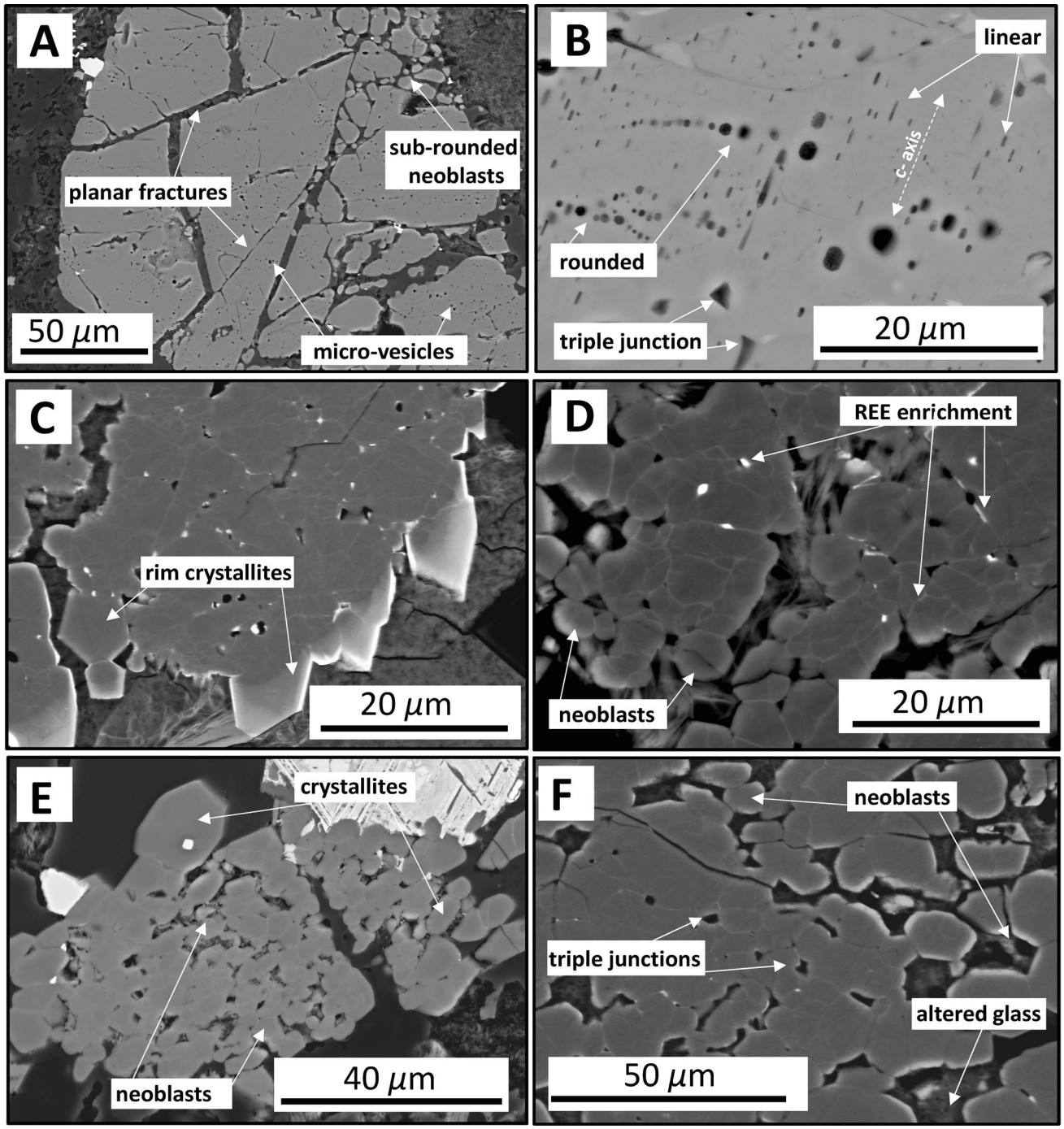

Fig. 7 Representative backscattered images showing apatite microstructures. **a** Apatite clast (clast-laden melt breccia; B47) with planar fractures (partly annealed) co-existing with small (< 5 μm) sub-rounded apatite neoblasts and micro-vesicles. **b** Example of apatite clast situated within impact melt (crystalline melt rock; B44) containing two morphological types of micro-vesicles (rounded/linear and elongate/parallel to *c*-axis). Triple junctions also present. **c**–**f** Apatite grains exhibiting a range of recrystallization textures. **c** Partial recrystallization (clast-laden breccia, B40) with euhedral crystallites along host rim. Rim crystallites enriched in REEs, inclusions of high REEs within micro-vesicles, triple junctions. **d**–**f** Completely recrystallized grains within clast-poor melt rocks with well-defined neoblasts and/or euhedral crystallites either semi-isolated or isolated from the host grain. Enrichment of REEs occurring along neoblast boundaries and as inclusions in micro-vesicles and within triple junctions

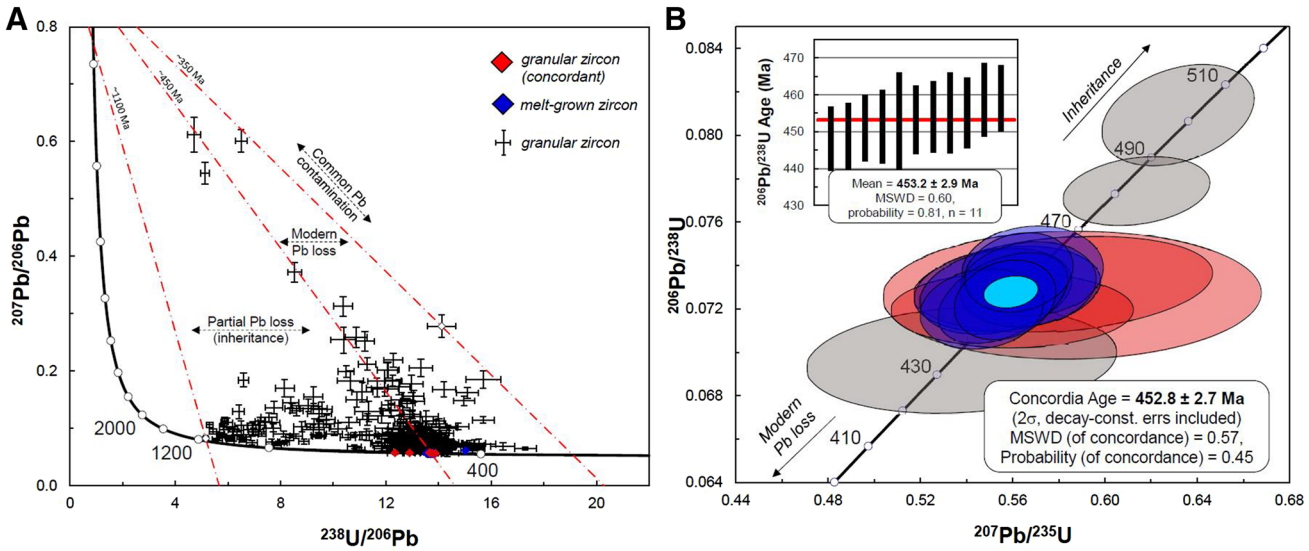

Fig. 8 LA-ICP-MS U–Pb zircon age calculations. All data provided in Table S4. **a** All zircon data ($n=377$) plotted on a Tera-Wasserburg concordia diagram showing an age distribution between ~ 1000 and 350 Ma. Blue diamonds designate analyses from melt-grown zircons; all other data points are from granular zircon grains. Red age vector regressions are anchored using the $^{207}Pb/^{206}Pb$ value from inherited feldspar clasts (0.9145). Analyses plotting between 1000 and 450 Ma are partially reset (i.e., exhibit variable degrees of inheritance); analyses between 450 and 350 Ma have undergone recent (post-impact Pb loss). Common Pb (PbC) incorporation is indicated by analyses that have higher $^{207}Pb/^{206}Pb$. **b** Wetherill diagram showing the calculated concordia age of 452.8 ± 2.7 Ma (MSWD 0.57, $p=0.45$, $n=11$) obtained from granular zircon (red ellipse) and impact melt-grown zircon (blue ellipse) with a corresponding weighted mean $^{206}Pb/^{238}U$ age of 453.2 ± 2.9 Ma (inset diagram). Black ellipses not included in calculation are representative of variable degrees of inheritance and modern Pb loss recorded in granular zircon grains

grain boundaries and triple junctions within REE-fluorapatite grains (e.g., Fig. 7d, f). These regions are enriched in Ce_2O_3, Nd_2O_3, La_2O_3, Y_2O_3, and silica relative to the darker (in BSE) interiors of individual neoblasts (Fig. S2). The variations in brightness of these regions correspond to increasing concentrations of Si and REEs, and a decrease in CaO and P_2O_5, consistent with the coupled substitution $REE^{3+} + Si^{4+} \leftrightarrow Ca^{2+}\ P^{5+}$ (Watson and Green 1981; Fig. S2). Although it is not possible to precisely determine the composition of this phase due to peak overlap and beam size, the increased P_2O_5 and presence of LREEs suggest that this phase is probably monazite [$(LREE)PO_4$].

LA-ICP-MS U–Pb geochronology

Zircon

A total of 377 analyses obtained from 120 zircon grains within clast-laden and clast-poor impact melt rocks were acquired for U–Pb geochronology. U and Th concentrations range between 13–900 ppm and 5–4000 ppm, respectively (Table S4). Dated grains are a mix of both newly-grown (igneous) grains crystallized from impact melt ($n=9$), and recrystallized mineral clasts inherited from the underlying basement ($n=111$). On a Tera-Wasserburg concordia diagram, the data is distributed between ~ 1100 and ~ 350 Ma, with a cluster of data points surrounding those on melt-grown zircons with concordant ages at ~ 450 Ma (Fig. 8). In Wetherill space, there is a large dispersion in the observed $^{207}Pb/^{235}U$ ratio due to the presence of common Pb (Fig. S4). As a result, no statistically robust linear discordia array can be calculated to obtain an upper intercept crystallization age, or a lower intercept impact age.

Of the 377 analyses obtained, only 14 analyses fall on concordia (Fig. 8b). Although the majority of zircon grains within all samples are variably reset, all concordant analyses are obtained from melt-grown zircon and granular zircon grains with impinging neoblasts that are within the basal impact melt zone and the lower aureole breccia (Fig. S4). Nine are from impact melt-grown zircon grains, while the other six are from granular zircons with impinging neoblasts (e.g., Fig. 6a, d). Excluding one melt-grown point inadvertently placed along a fracture, all melt-grown zircons yield a concordant U–Pb age of 453.1 ± 3.1 Ma (MSWD 1.16, $n=8$). Those analyses on domains within granular zircon, where neoblasts are impinging, are also concordant ($n=3$) and, excluding points that show evidence of inheritance and recent Pb-loss (black ellipses; Fig. 8b), yield a concordia age of 452.8 ± 2.7 Ma (MSWD 0.57) when combined with melt-grown grains. This corresponds to weighted average mean $^{206}Pb/^{238}U$ age of 453.2 ± 2.9 Ma (MSWD 0.60) ($n=11$) (Fig. 8b).

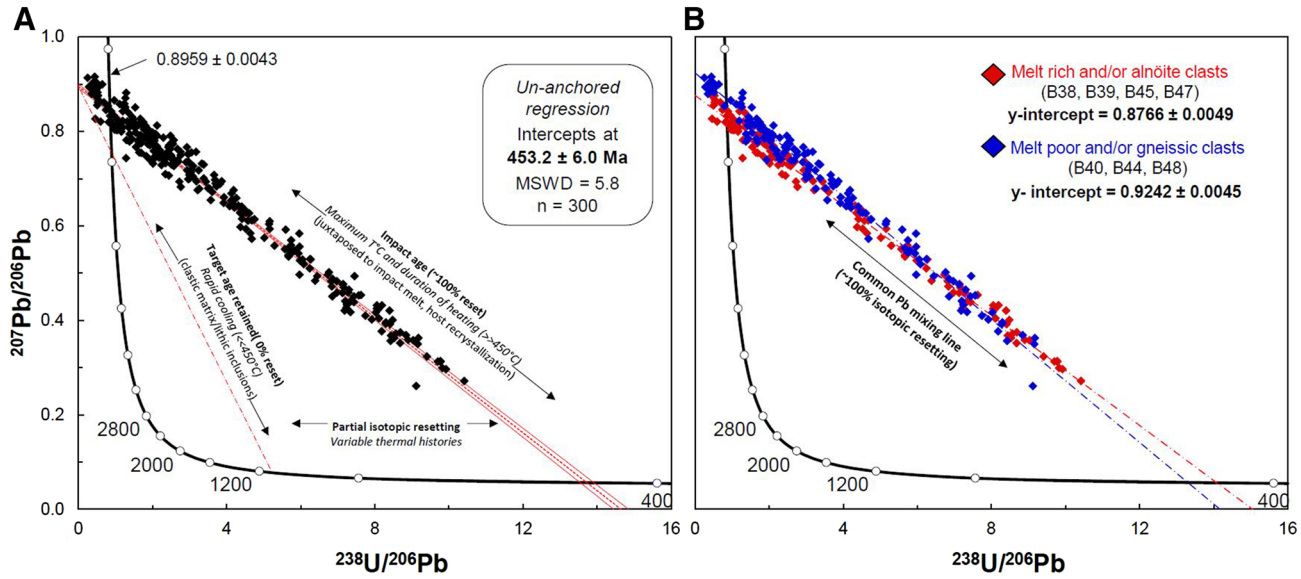

Fig. 9 LA-ICP-MS U–Pb concordia diagrams for apatite. Data provided in Table S5. **a** Inverse concordia showing the unanchored linear regression of all analyses ($n=300$) with a lower intercept age of 453.2 ± 6.0 Ma (MSWD 5.8, $n=300$), and a $^{207}Pb/^{206}Pb$ intercept of 0.8959 ± 0.0043. Also shown for comparison with previous studies is the typical "fan-like" or triangular distribution of isotopic ratios in apatite within suevites (see text for discussion). **b** Inverse concordia diagram of all analyses showing the variation in the $^{207}Pb/^{206}Pb$ intercept between apatite grains within different samples. Red diamonds represent data collected from apatites occurring within melt-rich samples and/or which contain alnöite clasts (B38, B39, B45, B47) which have a *y*-intercept value of 0.8766 ± 0.0049. Grains within melt-poor samples and/or that have gneissic clasts (B40, B48, B44) (blue diamonds) have an y-intercept of 0.9242 ± 0.0045. All data is uncorrected for common Pb

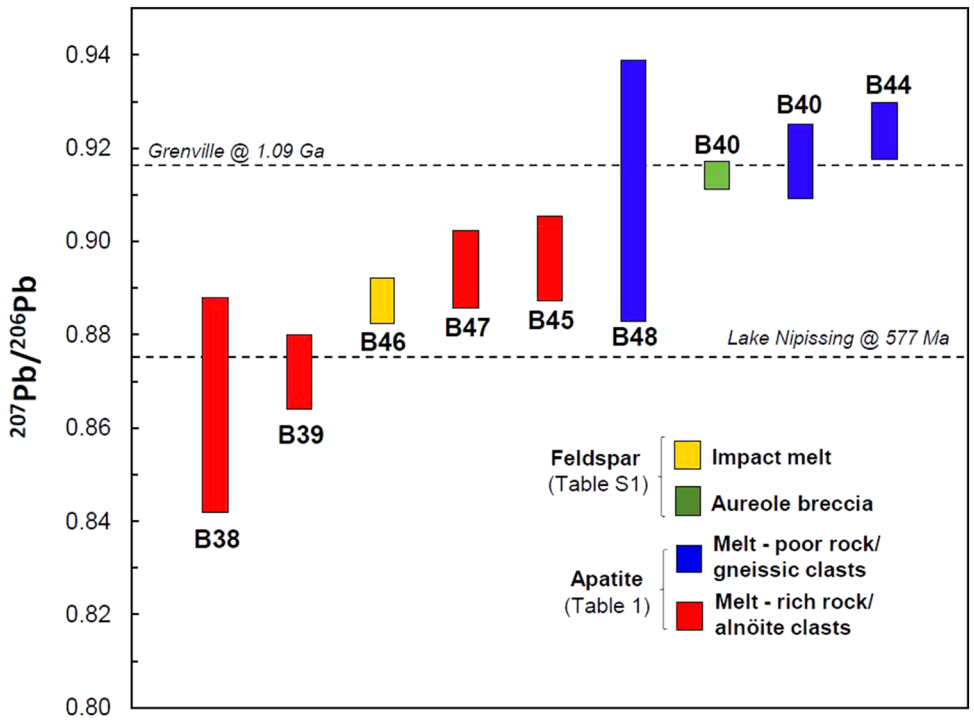

Fig. 10 Simplified plot showing the variation in $^{207}Pb/^{206}Pb$ recorded in feldspar and apatite grains from various samples (see inset legend)

There is a large dispersion of isotopic ratios recorded by zircon, interpreted to be the result of an interplay between (1) ancient, impact-related Pb loss, (2) inheritance or partial Pb loss, (3) common Pb contamination, and (4) recent Pb loss. This is clearly visualized on a Tera-Wasserburg diagram by plotting age vectors anchored with the initial

Table 1 $^{207}Pb/^{206}Pb$ intercept values for apatite grains from all lithologies

Sample	*y*-intercept	Lower intercept age (Ma)	Lithology	Lithic clast
B38	0.865 ± 0.023	440 ± 10	Clast-laden melt (50:50)	Gneissic
B39	0.8722 ± 0.0079	449 ± 17	Clast poor melt (90:10)	Gneissic
B40	0.9174 ± 0.0080	454 ± 13	Clast-rich melt (20:80)	Gneissic
B44	0.9239 ± 0.0060	456 ± 11	Clast-poor melt (95:5)	Gneissic
B45	0.8966 ± 0.0092	468 ± 38	Clast-poor melt (95:5)	Gneiss and alnöite
B47	0.8942 ± 0.0083	440 ± 6.0	Clast-laden melt (40:60)	Gneiss and alnöite
B48	0.911 ± 0.028	472 ± 16	Clast-rich melt (30:70)	Gneissic

All ages are inverse lower intercept ages calculated using a free regression

Ratios are melt:clast. *y*-intercept values correspond to initial $^{207}Pb/^{206}Pb$

$^{207}Pb/^{206}Pb$ recorded by feldspar clasts (Fig. 8a). The impact event is constrained by the age vector defined by those concordant points at 452.8 ± 2.7 Ma, which have neither inherited Pb, nor experienced any modern Pb loss. While there is likely to be a combination of inheritance, common Pb contamination and recent Pb loss, the data can be broadly grouped into three populations defined by the concordant analyses. Data points that fall to the left of the 450 Ma age vector, and to the right of the vector defined by the oldest data point at ~ 1100 Ma (~ 1136 ± 16 Ma), are representative of various degrees of inheritance. These partially preserve pre-impact radiogenic Pb. Those to the right of the impact age vector at ~ 450 Ma and to the left of the youngest age vector at ~ 350 Ma (329 ± 19 Ma), exhibit variable degrees of post-impact Pb loss towards an ill defined lower intercept.

This relationship is further demonstrated when considering points that fall on concordia (Fig. 8b; black ellipses). While several analyses from granular zircons (impinging domains; red ellipses) give the same age as melt-grown zircons (blue ellipses), two points show evidence of inheritance (i.e., higher $^{206}Pb/^{238}U$). Analyses with $^{206}Pb/^{238}U$ ages younger than those defined by the concordant cluster represent varying degrees of recent Pb loss (i.e., lower $^{206}Pb/^{238}U$). In both the older and younger age populations, there is no link between the recorded $^{206}Pb/^{238}U$ age and U or Th content that would indicate recent Pb loss associated with metamict domains.

Apatite

A total of 300 analyses were obtained from 100 individual (inherited) apatite grains within both clast-laden and clast-poor impact melt rocks. All data points define a linear array that reflect a mixing line between common Pb and radiogenic Pb (Fig. 9a). A raw, unanchored regression calculated using all the data yields a lower intercept age of 453.2 ± 6.0 Ma (MSWD 5.8) (Fig. 9a). To determine if the accuracy of this intercept could be improved by applying a common Pb correction, the regression was anchored using the initial $^{207}Pb/^{206}Pb$ values obtained from feldspar (Table S2). The $^{207}Pb/^{206}Pb$ ratio is distinct between newly-grown (igneous) feldspar grains within crystalline melt rock samples (weighted mean $^{207}Pb/^{206}Pb$ value of 0.8875 ± 0.0048) (Fig. S3a), and inherited grains within the thermal aureole (weighted mean $^{207}Pb/^{206}Pb$ value of 0.9145 ± 0.0030) (Fig. S3a). Anchoring the regression using a $^{207}Pb/^{206}Pb$ value of 0.8875 ± 0.0048 yields a lower intercept age of 453.0 ± 5.9 Ma, while a lower intercept age of 454.5 ± 5.9 Ma is obtained if the regression is anchored using a $^{207}Pb/^{206}Pb$ value of 0.9145 ± 0.003. Both intercept ages overlap within error of zircon, and are almost identical to that of the raw regression. However, given the variable $^{207}Pb/^{206}Pb$ signature recorded by both apatite and feldspar (see below; Fig. 10), the most accurate intercept age is considered to be that of the unanchored, raw regression. Thus, the lower intercept impact age recorded by apatite is 453.2 ± 6.0 Ma (MSWD 5.8, $n = 300$).

Similar to feldspar, a relationship is observed between the initial Pb composition recorded in apatite, the host lithology (i.e., clast-poor melt versus clast-laden impact melt in the aureole) and lithic clast content (i.e., gneissic versus alnöitic) (Fig. 9b). The free regression of the data set yields an initial $^{207}Pb/^{206}Pb$ intercept value of 0.8959 ± 0.0043 (Fig. 9a). This value is between that estimated using the Stacey and Kramers (1975) Pb isotope evolution model for the two basement lithologies (Grenville at 1.09 Ga, $^{207}Pb/^{206}Pb = 0.916$; Lake Nipissing alnöites: ~ 577 Ga, $^{207}Pb/^{206}Pb = 0.875$), and is between that obtained from metamorphosed (i.e., inherited) and new "igneous" feldspars (Fig. S3). If the $^{207}Pb/^{206}Pb$ intercepts are calculated separately for individual samples, a distinct variation in the y-intercept value, and corresponding lower intercept age, is apparent (Table 1; Fig. 10).

A free regression of points from apatite grains within melt-rich samples (samples B38, B39, B45) and those dominated by alnöite clasts (sample B47) yield *y*-intercept $^{207}Pb/^{206}Pb$ values of 0.865 ± 0.0023, 0.8722 ± 0.0079, 0.8966 ± 0.0092 and 0.8942 ± 0.0083, respectively (Table 1; Fig. 10). Plotted together, a *y*-intercept of

0.8766 ± 0.0049 is obtained (Fig. 9b), which is similar to that of melt-grown (igneous) feldspars (Fig. S3; Fig. 10). In contrast, apatite grains from melt-poor samples (samples B40, B48), and impact melt samples dominated by gneissic clasts (B44), yield initial Pb intercept values of 0.9174 ± 0.0080, 0.911 ± 0.028 and 0.9239 ± 0.0060, respectively (Table 1; Fig. 10). Considered together, this yields a *y*-intercept value of 0.9242 ± 0.0045 (Fig. 9b), which resembles the $^{207}Pb/^{206}Pb$ value of inherited feldspar grains within the aureole sample (Fig. S3). An age of 442 ± 6.7 Ma is obtained from the first population (red diamonds; Fig. 9b), while a lower intercept age of 467.1 ± 6.2 Ma is obtained from the second population (blue diamonds; Fig. 9b). The intercept ages obtained from these two common Pb composition populations are distinct, and considered together with the entire data set, explains the large MSWD (= 5.8) and the ± 6 Ma age uncertainty obtained in the raw regression.

Discussion

A refined isotopic age for the Brent impact structure

The application of in situ LA-ICP-MS U–Pb geochronology to apatite and zircon grains from clast-laden and clast-poor melt rocks has provided the first U–Pb age for the Brent impact structure. Analyses of both impact melt-grown and impact-recrystallized (i.e., granular) zircon grains yield a concordia age of 452.8 ± 2.7 Ma (MSWD 0.57, $n = 11$) (Fig. 8b). Apatite grains experienced extensive isotopic resetting during the impact, with negligible preservation of pre-impact radiogenic Pb. All analyses define a linear array with a lower intercept age of 453.2 ± 6.0 Ma (MSWD 5.8, $n = 300$) (Fig. 9a), which is within error of zircon. Given that the age obtained from zircon is derived from concordant points from both impact melt-grown and completely recrystallized grains, the age from zircon is considered as the most robust estimate for the timing of the Brent-forming impact event. However, it should be pointed out that ages from both phases overlap within error and, although the most precise age is obtained from zircon, this is primarily due to the presence of melt-grown zircons, and apatite would likely have provided the most accurate age in their absence. The ages obtained from both zircon and apatite are consistent with the minimum biostratigraphic age of Upper Ordovician (Black Riveran–Early Trentonian) obtained from post-impact fossiliferous limestones that fill the crater (Fig. 2; Grahn and Ormö 1995).

The effect of post-depositional recrystallization on the U–Pb systematics of apatite and zircon

In addition to providing an impact age for Brent, this study also provides insight into the isotope systematics of zircon and apatite under impact-related *P–T–t* conditions, particularly their response to thermal recrystallization of impactite lithologies.

LA-ICP-MS U–Pb geochronology of shocked zircon typically produces complex discordia arrays, with Pb loss correlating with the degree of shock metamorphism, from which lower intercept impact ages can be obtained (Kamo et al. 1996; McGregor et al. 2018; Schmieder et al. 2019). Moreover, recent studies highlight the observation that metamict domains within inherited zircon grains are more chronometrically reset compared to crystalline zircon, where radiation damage provides fast diffusion pathways that facilitate enhanced Pb loss during impact (McGregor et al. 2019a; Schmieder et al. 2019). However, recent Pb loss from sub-micron neoblasts within granular zircon (Kamo et al. 2011), along with post-impact Pb loss and common Pb contamination within U-rich metamict domains (McGregor et al. 2019a, 2020), can significantly compromise the reliability of lower intercept ages in zircon.

In this study, an impact age is constrained by concordant analyses from impact melt-grown zircon grains and recrystallized inherited grains (i.e., granular zircon). We propose that isotopic resetting of zircon grains at Brent was driven by the prolonged heating of inherited zircon grains within the basal melt zone, and associated thermal recrystallization (i.e., contact metamorphism) of the upper and lower aureole units that facilitated the generation of melt-grown zircons, and complete Pb loss from several recrystallized grains (Fig. 8b). Besides the melt-grown zircons (Fig. 5), all relic zircon grains are granular (i.e., recrystallized) (Fig. 6). This suggests that heating was both at adequate temperatures and of sufficient duration to induce extensive recrystallization of inherited zircon grains, and facilitate new zircon growth within impact melt. However, based on the preservation of inherited, pre-impact radiogenic Pb within analyses on the majority of granular zircons (Fig. 8), it is apparent that recrystallization did not facilitate complete Pb loss during the impact event. This suggests that, in contrast to apatite, Pb loss during impact-induced recrystallization is highly heterogenous in zircon.

An additional difficulty of dating granular zircon is the presence of common Pb and recent (post-impact) Pb loss. In this study, common Pb contamination exhibited by zircon (i.e., high $^{207}Pb/^{206}Pb$; Fig. 8a) is restricted to grains that experienced impact-induced recrystallization, and is absent in analyses of melt-grown zircons, and regions with impinging neoblasts (i.e., Fig. 8a). This is interpreted to be

the result of variable amounts of common Pb within impact melt situated between individual zircon neoblasts.

Deciphering the mechanism responsible for the observed recent Pb loss, as suggested by the ~ 350 Ma age vector (Fig. 8a), is more challenging. Unlike previous studies, where post-impact Pb loss corresponds to relic grains that preserve pre-impact metamict domains (McGregor et al. 2020), all analyses that record recent Pb loss in this study are from recrystallized grains (Fig. 8). While there is evidence for the metamictization of impact melt-grown zircons, as suggested by both the high U concentration of these grains and minor metamict textures (Fig. 5b), all impact-melt zircon grains plot on concordia at 450 Ma and exhibit no recent Pb loss. Moreover, there is no observed correlation between U concentration and recorded $^{206}Pb/^{238}U$ ages. This is in contrast to previous studies, where recent (post-impact) Pb loss was strongly controlled by the level of radiation damage in relic grains (i.e., McGregor et al. 2019a). Given that those analyses with younger $^{206}Pb/^{238}U$ ages are all from granular zircons, rather than pre-impact metamict domains in relic grains, we interpret this to be the result of recent Pb loss from sub-micron zircon neoblasts (Kamo et al. 2011), rather than as a result of recent Pb loss from pre-impact metamict domains (Schmieder et al. 2019; McGregor et al. 2019, 2020).

It should also be mentioned that the ~ 350 Ma age vector defining post-impact Pb-loss in zircon (Fig. 8a) broadly coincides with K–Ar ages between 300 and 400 Ma obtained from strongly shocked to melted K-feldspars (Hartung et al. 1971). These younger ages are recorded by strongly altered and shocked K-feldspars, with the younger ages attributed to a post-impact alteration event, rather than recent argon-loss from shocked domains. However, given the higher blocking temperature of crystalline zircon (900 °C) compared to the K–Ar system (< 300 °C), any post-impact thermal event capable to resetting the Ar/Ar system is unlikely to have reset the U–Pb system in zircon and, if so, any Pb-loss recorded by zircon in this event would have been recorded by apatite (closure temperature ~ 450 °C), which is not apparent here.

In regards to apatite, the results from this study are distinct from previous investigations, where the U–Pb dating of relict apatite typically shows that grains experience variable degrees of isotopic resetting (cf., Fig. 9a; McGregor et al. 2018, 2019a, 2020). In these studies, apatites within impact melt-bearing breccias from impact structures developed in crystalline basement display a "fan-like" (or triangular) distribution of isotopic ratios depending on grain proximity to impact melt, from which both basement (i.e., target) ages and impact ages can be obtained (McGregor et al. 2018, 2019a; Fig. 9a). While a similar "fan-like" isotopic distribution is obtained for structures formed within sedimentary targets, impact-age resetting is recorded by apatite grains within samples that experienced post-depositional matrix recrystallization at temperatures > 450 °C (Walton et al. 2017; McGregor et al. 2020). At Brent, which is a simple (~ 3.4 km diameter) crater formed in crystalline basement, the effects of prolonged heating and thermal recrystallization of the upper and lower aureole units have strongly influenced the degree of isotopic resetting in apatite. Prolonged temperatures > 450 °C appear to have been sufficient to induce extensive Pb loss in relic grains, with little evidence of inherited ages from the protolith (Fig. 9a). This is in sharp contrast to the isotopic variability recorded in zircon (Fig. 8a). While zircon gives the most precise age due to the presence of impact-melt zircons ($n = 8$) and concordant ages from granular domains ($n = 3$), the majority of analyses indicate highly heterogenous U–Pb ratios. Therefore, similar to previous U–Pb chronological studies of apatite within impact melt-bearing breccias (McGregor et al. 2020), we conclude that apatite is the more viable impact chronometer, particularly in the absence of melt-grown accessory phases.

While the application of LA-ICP-MS has previously proven challenging for dating impact-affected zircon, the technique has been shown to be particularly useful for dating apatite within impact melt-bearing breccias (e.g., suevites). Given the complicated nature of impactite lithologies, in situ analysis allows ages to be correlated with textural context, where the degree of isotopic resetting can be related to a given grain's proximity to impact melt, or as determined in this study, thermal recrystallization of the host lithology. The viability of apatite as an impact chronometer has, with the addition of this study, been facilitated primarily by the application of in situ LA-ICP-MS on inherited phases within impact melt-bearing breccias (McGregor et al. 2018, 2019a, 2020). While both SIMS and LA-ICP-MS enable specific targeting of reset domains (i.e., recrystallized, melt-grown), LA-ICP-MS has a much higher data throughput that enables a larger number of analyses to be obtained. This provides a more representative record of the isotope systematics experienced by various accessory phases during the variable *P–T–t* histories realized by impact events. This is clearly displayed in this study, where the selection of > 300 spot analyses from zircon and apatite within the same lithologies has demonstrated that, under the same *P–T–t* conditions, these phases record distinct U–Pb isotope systematics.

An additional interesting outcome of this study is the documentation of impact melt-grown zircon and apatite from the basal impact melt zone. Newly crystallized zircons are generally thought to be generated within large impact melt sheets in complex impact structures (e.g., Manicouagan; Hodych and Dunning 1992). The documentation of newly-grown impact melt zircon and apatite at Brent suggests that dateable U–Pb geochronometers can be generated in simple impact craters, and are not restricted to larger complex structures possessing larger coherent impact melt bodies.

Initial $^{207}Pb/^{206}Pb$ signature of impact melt recorded by feldspar and apatite

Apatite and feldspar record similar $^{207}Pb/^{206}Pb$ ratios, with systematic differences recorded in grains depending on petrogenetic setting (Fig. 9b; Fig. 10). As indicated by the $^{207}Pb/^{206}Pb$ ratios obtained from feldspar, the initial isotopic composition differs considerably between inherited grains within the metamorphic aureole (0.9145 ± 0.0030) and impact melt-grown grains (0.8875 ± 0.0048) (Fig. S3; Fig. 10). The different $^{207}Pb/^{206}Pb$ ratios between these samples is interpreted as being indicative of mixing and subsequent re-equilibration of impact melt derived from both Grenville gneisses and Lake Nipissing alnöites.

The same $^{207}Pb/^{206}Pb$ isotopic heterogeneity is also recorded in inherited apatite grains, where a systematic variation in the $^{207}Pb/^{206}Pb$ intercept exists between samples depending on the amount of impact melt and type of lithic clasts (Table 1; Fig. 9b; Fig. 10). In samples with > 50% impact melt and/or where alnöite clasts are abundant, apatite grains record an initial Pb value of 0.8766 ± 0.0049, which approximates that of the re-equilibrated $^{207}Pb/^{206}Pb$ signature recorded by impact melt-grown feldspars (Fig. 9b; Fig. 10; Fig. S3). In contrast, grains within melt-poor samples (< 50%) (B40, B48), and within melt-rich samples containing gneissic fragments (B44), yield an initial $^{207}Pb/^{206}Pb$ intercept of 0.9242 ± 0.0045, which is similar to the initial Pb obtained from the inherited aureole feldspars (Figs. 9b; Fig. S3; Fig. 10). Retention of initial Pb signatures has also been documented in apatite from the Steen River impact structure (McGregor et al. 2020), where apatite grains occurring as mineral clasts within clastic matrices, or as inclusions in lithic clasts, retain the same inital$^{207}Pb/^{206}Pb$ composition as co-existing inherited feldspars grains.

While the predominant target rock involved in the impact at Brent was mesoperthitic gneiss and minor gabbroic coronites, the contribution of alnöite dykes to melt generation has previously been suggested by Currie (1971) and Hartung et al. (1971). However, whole rock geochemistry by Grieve (1978) and Palme et al. (1981) indicates that the bulk chemistry of the melt has a composition indicative of mixing between mesoperthitic gneiss and L-Chondrite material, with little or no contribution from alnöite. In the present study, feldspar $^{207}Pb/^{206}Pb$ values obtained from impact melt feldspars and apatite grains provide strong evidence for mixing between a significant component of the younger (~ 577 Ma) Lake Nipissing alnöites and the older (~ 1.0 Ga) Grenville gneisses. Although the bulk geochemistry of the impact melt indicates mixing of ~ 98.5% gneiss and 1.5% L-Chrondrite (Grieve 1978; Palme et al. 1981), the $^{207}Pb/^{206}Pb$ ratio of the projectile was evidently not retained within feldspars crystallized from the impact melt. Given a typical $^{207}Pb/^{206}Pb$ value of ~ 1.10 for a chondritic meteorite (Connelly et al. 2017), an initial Pb value > 0.9145 would be expected for mixing with a component containing a primordial Pb signature. Thus, while the chemistry of the melt confirms the involvement of an L-Chondritic component, its $^{207}Pb/^{206}Pb$ signature was evidently not retained.

Trace element heterogeneity in recrystallized apatite

Apatite group minerals ($REE,Ca_5(PO_4)_3(F,OH,Cl)$) can accommodate elements from over half the periodic table into their crystal structure, with calcium occupying two sites: Ca_1 (1.18 Å) and Ca_2 (1.06 Å). This permits coupled substitutions with numerous trace elements, such as Na, Mg, Mn, REEs, U, Th and Pb (Spear and Pyle 2000; Prowatke and Klemme 2006). In this study, we observe regions of high BSE contrast along grain boundaries of individual neoblasts, at the tips of euhedral rim crystallites, along triple junctions, and as inclusions within micro-vesicles. These regions are enriched in light rare earth elements (LREEs; notably Y_2O_3, Ce_2O_3, Nd_2O_3 and La_2O_3) and silica relative to the interior of neoblasts (Fig. 7; Fig. S2). The positive correlation of LREEs with Si suggests a coupled substitution of $Si^{4+} + LREE^{3+} = P^{5+} + Ca^{2+}$ that is consistent with the formation of monazite (Pan and Fleet 2002; Hughes and Rakovan 2015).

Chemical heterogeneities have recently been documented in apatite grains from the Paasselkä impact structure, Finland, where elongate, oriented inclusions of $(Mg, Fe)_2(PO_4)$ are found in recrystallized apatite grains. The authors invoke a "phase separation" formation mechanism (Kenny et al. 2020). In this study, REE-enrichments are restricted to neoblast grain boundaries, rim crystallites and triple junctions (Fig. 7; Fig. S2). This suggests that enrichment occurred in response to recrystallization of the host grain rather than by subsequent hydrothermal alteration. Similar inclusions/enrichments of REE and MgFe phosphates have been documented in apatite grains in response to fluid-induced metasomatism via dissolution-re-precipitation (Harlov et al. 2002, 2005; Seifert et al. 2010). The observed textures in this study differ from those showing dissolution–precipitation features, where apatite grain boundaries and crystal defects are depleted in REEs in response to their mobilization during fluid interaction (Harlov et al. 2002, 2005; Putnis 2009). Moreover, the partition coefficients of REEs in apatite are strongly affected by melt composition (Watson and Green 1981). Given that the basement lithologies at Brent (Grenville gneisses and Lake Nipissing alnöites) are known to contain REE-rich lithologies (Currie 1971; Cullers and Medaris 1977; Bleeker et al. 2011), REEs within apatite grains derived from these lithologies would become less compatible during impact-induced (thermal) recrystallization, with elemental instabilities between the

Table 2 Terrestrial impact structures with well-constrained ages between 450 and 455 Ma

Name	Country	Diameter km	Age Ma	Technique(s)	References
Brent	Canada	3.4	452.8 ± 2.7	U–Pb LA-ICP-MS	This work
Glasford	USA	4	455 ± 2	Stratigraphic	Monson et al. (2019)
Kärdla	Estonia	4	455 ± 1	Stratigraphic	Grahn et al. (1996)
Lac La Moinerie	Canada	8	453 ± 5	U–Pb LA-ICP-MS	McGregor et al. (2019a)
Lockne	Sweden	7.5	455 ± 1	Stratigraphic	Ormö et al. (2014)
Mälingen	Sweden	0.7	455 ± 1	Stratigraphic	Grahn et al. (1996)
Pilot Lake	Canada	6	450 ± 2	Ar–Ar	Bottomley et al. (1990)

host and recrystallized domains of apatite resulting in the precipitation of new phases. Based on these observations and that of Kenny et al. (2020), it is apparent that the composition of the parent grain formed in the target lithologies will control the composition of the phase precipitated during impact-induced recrystallization. However, although the influence of impact-induced recrystallization probably affects the chemical heterogeneity of apatite in terrestrial impact structures, the documentation of chemical heterogeneity in recrystallized apatite is limited. More studies of both naturally and experimentally shocked apatite are required to determine the mechanisms responsible, whether it be phase separation/precipitation resulting from recrystallization or dissolution–precipitation during metasomatism.

Delivery of the larger L-Chondrite asteroid fragments to earth

An age of 452.8 ± 2.7 Ma places the Brent-forming impact event at or near the Sandbian–Katian boundary in the Late Ordovician. The Ordovician was a period of enhanced debris flux to Earth that has been attributed to the L-Chondrite parent body (150–200 km original diameter) breakup (LCPB), which occurred in the asteroid belt at ~ 466 Ma (Korochantseva et al. 2007; Schmitz et al. 2008; Lindskog et al. 2017). Initial material delivered to Earth was fine dust, micrometeorites, and smaller meteorites, which occurred soon (0.3–2.0 Ma) after breakup due to short transfer times (Schmitz et al. 2019). Delivery of the larger L-Chondrite fragments to Earth took place later, compatible with a more protracted (2.0–20 Ma) transfer period (Zappala et al. 1998).

At least seven terrestrial impact craters have well-constrained ages between 450 and 455 Ma (Table 2). Other potential members of the cluster include Ames, Calvin, Decorah (USA), Charlevoix, Clearwater East, Lac Couture, Slate Islands, Tunnunik (Canada), Ilyinets (Ukraine) and Granby, Hummeln and Tvären (Sweden) (Earth Impact Database 2020). However, these require further age refinements to be confirmed as cluster members. Cluster membership also requires the duration of the larger asteroid delivery window to be better constrained (e.g., 460 to 450 Ma). The impact structures in Table 2 are relatively small (< 10 km diameter) with probable projectile diameters < 0.5 km, but some of the potential cluster members are larger (Charlevoix, Slate Islands, and Clearwater East are 54, 30 and 26 km in diameter, respectively). Despite the small size of many of the Sandbian–Katian structures listed in Table 2, it is not reasonable to preclude the possibility of larger structures having been generated that have not yet been recognized and/or dated. Additional cluster candidates could be buried, or have been destroyed via subduction or other recycling processes on our active planet, or have poorly defined ages that currently place them outside this time window.

Conclusions

1. In situ LA-ICP-MS U–Pb geochronology performed on apatite and zircon within thermally recrystallized clast-rich and clast-poor impact melt samples from the Brent impact structure have provided a refined age of formation. A concordia age of 452.8 ± 2.7 Ma (MSWD 0.57, $n = 11$) obtained from impact melt-grown and recrystallized (inherited) zircon grains is considered the best-estimate impact age for Brent. Apatite records an impact age within error of zircon, with all grains exhibiting more extensive isotopic resetting, forming a linear array with a well-defined lower intercept age of 453.2 ± 6.0 Ma (MSWD 5.8; $n = 300$).
2. This places the impact event at or near the Sandbian–Katian boundary during the Late Ordovician. Brent joins seven well-dated, and up to a potential total of 20 or more, terrestrial impact structures that were generated during a period of enhanced projectile flux to Earth during delivery of the larger fragments from the L-Chondrite disruption event, some 5–10 Ma after breakup.
3. Inherited, impact-recrystallized zircon records highly heterogenous isotopic ratios due to an interplay of inheritance, common Pb contamination and recent Pb loss. Completely recrystallized zircon grains preserve vari-

able pre-impact radiogenic Pb; impact melt situated between non-impinging neoblasts contributes to common Pb contamination; and recent Pb loss occurs from sub-micron neoblastic domains.

4. The inclusion of apatite grains within the impact melt zone, combined with the prolonged heating of grains within thermally recrystallized clast-laden impact melt rocks, facilitated extensive isotopic resetting and limited preservation of initial radiogenic Pb. Unlike previous U–Pb studies of apatite within suevites, a "fan-like" distribution of the U–Pb ratios is not observed. Instead, all apatite grains define a linear array with an intercept age that overlaps within error of zircon. Our results support previous suggestions that isotopic resetting in apatite is primarily thermally driven and facilitated by grain–melt interactions during heating and/or recrystallization of host impactite lithologies.
5. Feldspar and apatite $^{207}Pb/^{206}Pb$ compositions provide evidence for isotopic re-equilibration of the impact melt sheet at Brent via mixing of Grenville gneisses and Lake Nipissing alnöites. No record of an initial $^{207}Pb/^{206}Pb$ composition of the L-Chondrite projectile involved in the impact event has been retained within the impact melt zone.
6. The observation of impact melt-grown zircon and apatite within clast-poor melt rocks and crystalline melt rocks at Brent demonstrates that their formation is not restricted to larger, complex craters as previously thought.

Acknowledgements This research was supported by Natural Sciences and Engineering Research Council of Canada (NSERC) and Canada Foundation for Innovation (CFI) grants to McFarlane and Spray. We thank Brandon Boucher for assistance in the Laser Ablation lab at UNB and Tom Cole for providing the topographic data. An earlier version of this work was improved by thoughtful and constructive reviews from James Darling, an anonymous reviewer, and Editor Daniela Rubatto. Planetary and Space Science Centre contribution 160.

References

Alwmark C, Ferrière L, Holm-Alwmark S, Ormö SJ, Leroux H, Sturkell E (2015) Impact origin for the Hummeln structure (Sweden) and its link to the Ordovician disruption of the L chondrite parent body. Geology 43:279–282

Bergström SM, Schmitz B, Liu HP, Terfelt F, McKay RM (2018) High resolution δ13C core chemostratigraphy links the Decorah impact structure and the Winneshiek Konservat-Lagerstatte to the Darriwilian global influx of meteorites. Lethaia 51:504–512

Bleeker W, Dix GR, Davidson A, LeCheminant A (2011) Tectonic evolution and sedimentary record of the Ottawa-Bonnechere Graben: Examining the Precambrian and Phanerozoic history of magmatic activity, Faulting and sedimentation. GACMAC 2011 Field Trip Guidebook

Bottomley RJ, York D, Grieve RAF (1990) ^{40}Argon–^{39}Argon dating of impact craters. Proc Lunar Planet Sci Conf 20:421–431

Chew DM, Petrus JA, Kamber BS (2014) U-Pb LA-ICP-MS dating using accessory mineral standards with variable common Pb. Chem Geol 363:185–199

Cooper RA, Sadler PM, Hammer O, Gradstein FM (2012) The Ordovician period. In: Gradstein FM, Ogg JG (eds) The geologic time scale, vol 2. Schmitz MD, Ogg GM), pp 489–523

Connelly JN, Bollard J, Bizzarro M (2017) Pb-Pb chronometry and the early Solar System. Geochim Cosmochim Acta 201:345–363

Cullers RL, Medaris G (1977) Rare earth elements in carbonatite and cogenetic alkaline rocks: examples from Seabrook Lake and Callander Bay, Ontario. Contrib Mineral Petrol 65:143–153

Currie KL (1971) A study of potash fenitization around the Brent Crater, Ontario—a Paleozoic alkaline complex. Can Jour Earth Sci 8:481–497

Erickson TM, Timms NE, Kirkland CL, Tohver E, Cavosie AJ, Pearce MA, Reddy SM (2017) Shocked monazite chronometry: integrating microstructural and in situ isotopic age data for determining precise impact ages. Contrib Mineral Petrol 172:11

Dence MR (1964) A comparative structural and petrographic study of probable Canadian meteorite craters. Meteoritics 2:249–270

Dence MR (1965) The extraterrestrial origin of Canadian craters. Annals New York Acad Sciences 123:941–969

Dence MR (1968) Shock zoning at Canadian craters: petrography and structural implications. In: French BM, Short NM (eds) Shock metamorphism of natural materials. Mono Book Corporation, Baltimore, pp 169–184

Dence MR (1971) Impact melts. J Geophys Res 76:5552–5565

Dence MR (2017) On critical observations that constrain models of terrestrial hypervelocity impact craters. Meteorit Plan Sci 52:1285–1299

Dickin AP, Strong JWD (2019) Nd isotope mapping of the Grenvillian Allochthon Boundary Thrust in Algonquin Park, Canada. Can J Earth Sci 56:101–110

Earth Impact Database. http://www.passc.net/EarthImpactDatabase. Accessed Feb 2020

French BM, McKay RM, Liu HP, Briggs DEG, Witzke BJ (2018) The Decorah structure, northeastern Iowa: geology and evidence for formation by meteorite impact. Bull Geol Soc Am 130:11–12

Goderis S, Vleminckx B, Paquay FS, Chackrabarti V, Renson V, Debaille W, Sluyts F, Vanhaecke F, Spray JG, Jacobsen SB, Claeys P (2010) The geochemistry of the Brent impact structure, Ontario. In: Goldschmidt Conf Abstr A340

Grahn Y, Ormö J (1995) Microfossil dating of the Brent meteorite crater, southeast Ontario, Canada. Rev Micropaleo 38:131–137

Grahn Y, Nõlvak J, Paris F (1996) Precise chitinozoan dating of Ordovician impact events in Baltoscandia. J Micropaleo 15:21–35

Grieve RAF (1978) The melt rocks at Brent crater, Ontario, Canada. Proc Lunar Plan Sci Conf 9:2579–2608

Harlov AE, Wirth R, Förster HJ (2005) An experimental study of dissolution-reprecipitation in fluorapatite: fluid infiltration and the formation of monazite. Contrib Mineral Petrol 150:268–286

Harlov AE, Andersson UB, Förster HJ, Nyström JO, Dulski P, Broman C (2002) Apatite-monazite relations in the Kirrunavaara magnetite-apatite ore, northern Sweden. Chem Geol 191:47–72

Hartung JB, Dence MR, Adams JAS (1971) Potassium-Argon dating of shock metamorphosed rocks from the Brent impact crater, Ontario, Canada. J Geophys Res 76:5437–5448

Hauser N, Reimold WU, Cavosie AJ, Crósta AP, Schwarz WH, Trieloff M, Da Silva Maia De Souza C, Pereira LA, Rodreigues E, Brown M (2019) Linking shock textures revealed by BSE, CL and EBSD with U-Pb data (LA-ICP-MS and SIMS) from zircon from the Araguainha impact structure, Brazil. Meteorit Planet Sci 54:2286–2311

Heaman LM (2008) The application of U-Pb geochronology to mafic, ultramafic and alkaline rocks: an evaluation of three mineral standards. Chem Geol 261:43–52

Hodych JO, Dunning GR (1992) Did the Manicouagan impact trigger end-of-Triassic mass extinction? Geology 20:51–54

Horstwood MSA (2008) Data reduction strategies, uncertainty assessment, and resolution of LA-(MC-)ICP-MS isotope data. Min Assoc Canada Short Course 40:283–303

Hughes JM, Rakovan JF (2015) Structurally robust, chemically diverse: apatite and apatite supergroup minerals. Elements 11:165–170

Innes MJS (1964) Recent advances in meteorite crater research at the Dominion Observatory, Ottawa, Canada. Meteoritics 2:219–242

Kamo SL, Krogh TE, Kumarapeli PS (1995) Age of the Grenville dyke swarm, Ontario-Quebec: implications for the timing of Iapetus rifting. Can J Earth Sci 32:273–280

Kamo SL, Reimold WU, Krogh TE, Colliston WP (1996) A 2.023 Ga age for the Vredefort impact event and a first report on shock metamorphosed zircons in pseudotachylitic breccias and Granophyre. Earth Planet Sci Lett 144:369–387

Kamo SL, Lana C, Morgan JV (2011) U-Pb ages of shocked zircon grains link distal K-Pg boundary sites in Spain and Italy with the Chicxulub impact. Earth Planet Sci Lett 310:401–408

Kay GM (1942) Ottawa-Bonnechere Graben and Lake Ontario homocline. Bull Geol Soc Am 53:585–646

Kenny GG, Morales LF, Whitehouse MJ, Petrus JA, Kamber BS (2018) The formation of large neoblasts in shocked zircon and their utility in dating impacts. Geol Soc Am 45:1003–1006

Kenny GG, Karlsson A, Schmieder M, Whitehouse MJ, Nemchin AA, Bellucci JJ (2020) Recrystallization and chemical changes in apatite in response to hypervelocity impact. Geology 48:19–23

Korochantseva EV, Trieloff M, Lorenz CA, Buykin AI, Ivanova MA, Schwarz WH, Hopp J, Jessberger EK (2007) L-chondrite asteroid breakup tied to Ordovician meteorite shower by multiple isochron ^{40}Ar–^{39}Ar dating. Meteorit Planet Sci 42:113–130

Kramers JD, Tolstikhin IN (1997) Two terrestrial lead isotope paradoxes, forward transport modelling, core formation and the history of the continental crust. Chem Geol 139:75–110

Lindskog A, Costa MM, Rasmussen CMO, Connelly JN, Eriksson ME (2017) Refined Ordovician timescale reveals no link between asteroid breakup and biodiversification. Nature 8:1–8

Lozej GP, Beales FW (1975) The unmetamorphosed sedimentary fill of the Brent meteorite crater, southeastern Ontario. Can J Earth Sci 12:606–628

McFarlane CR, Luo Y (2012) U-Pb Geochronology using 193 nm Excimer LA-ICP-MS optimized for in situ accessory mineral dating in thin sections. Mod Anal Fac 39:158–172

McGregor M, McFarlane CRM, Spray JG (2018) In situ LA-ICP-MS apatite and zircon U-Pb geochronology of the Nicholson Lake impact structure, Canada: shock and related thermal effects. Earth Planet Sci Lett 504:185–197

McGregor M, McFarlane CRM, Spray JG (2019a) Multiphase U-Pb geochronology and shock analysis of apatite, titanite, and zircon from the Lac La Moinerie impact structure. Canada Contrib Mineral Petrol 174:62

McGregor M, Erickson TM, Spray JG (2019b) Recrystallization and micro-twinning in apatite and titanite from the Lac La Moinerie impact structure, Canada: implications for U–Pb impact chronology. Large Meteor Impacts IV Abst #5099

McGregor M, Walton EL, McFarlane CRM, Spray JG (2020) Multiphase U–Pb geochronology of sintered breccias from the Steen River impact structure, Canada: mixed target considerations for a Jurassic-Cretaceous boundary event. Geochim Cosmochim Acta 274:136–156

Meldrum A, Boatner LA, Weber WJ, Ewing RC (1998) Radiation damage in zircon and monazite. Geochim Cosmochim Acta 62:2509–2520

Millman PM, Liberty BA, Clark JF, Willmore PL, Willmore, Innes MJS (1960) The Brent Crater. Dominion Observatory Pub., Ottawa 24, 43 p

Milstein RL (1988) Impact origin of the Calvin cryptoexplosive disturbance, Cass County, Michigan. Michigan Dept Nat Res Geol Surv Div Rep Investig 28:1–33

Monson CL, Sweet D, Segvic B, Zanoni G, Balling K, Wittmer JM, Ganis R, Cheng G (2019) The Late Ordovician (Sandbian) Glasford structure: a marine-target impact crater with a possible connection to the Ordovician meteorite event. Meteorit Planet Sci 54:2927–2950

Moser DE, Cupelli CL, Barker IR, Flowers RM, Bowman JR, Wooden J, Hart JR (2011) New zircon shock phenomena and their use for dating and reconstruction of large impact structures revealed by electron nanobeam (EBSD, CL, EDS) and isotopic U-Pb and (U–Th)/He analysis of the Vredefort dome. Can J Earth Sci 48:117–139

O'Connell-Cooper CD, Dickin AP, Spray JG (2012) The Manicouagan impact melt sheet: evidence for isotopic homogenization with limited assimilation. Earth Planet Sci Lett 335–336:48–58

Onorato PIK, Uhlmann DR, Simonds CH (1978) The thermal history of the Manicouagan impact melt sheet, Quebec. J Geophys Res 83:2789–2798

Ormö J, Sturkell E, Alwmark C, Melosh J (2014) First known terrestrial impact of a binary asteroid from a main belt breakup event. Sci Rep 4:6724

Paces JB, Miller JD (1993) Precise U-Pb ages of Duluth Complex and related mafic intrusions, Northeastern Minnesota—geochronological insights to physical, petrogenetic, paleomagnetic, and tectonomagmatic processes associated with the 1.1 Ga Midcontinent Rift System. J Geophys Res 98:13997–14013

Palme H, Grieve RAF, Wolf R (1981) Identification of the projectile at the Brent crater and further considerations of projectile types at terrestrial craters. Geochim Cosmochim Acta 45:2417–2424

Pan Y, Fleet ME (2002) Compositions of the apatite-group minerals: substitution mechanisms and controlling factors. Rev Mineral Geochem 48:13–49

Papapavlou K, Darling JR, Moser DE, Barker IR, White LF, Lightfoot PC, Storey CD, Dunlop J (2018) U-Pb isotopic dating of titanite microstructures: potential implications for the chronology and identification of large impact structures. Contrib Min Pet 173:1–15

Paton C, Hellstrom J, Paul JW, Hergt J (2011) Iolite: freeware for the visualization and processing of mass spectrometric data. J Analyt Atom Spectrom 26:2508–2518

Petrus JA, Kamber BS (2012) VizualAge: a novel approach to laser ablation ICP–MS U-Pb geochronology data reduction. Geostand Geoanalyt Res 36:247–270

Prowatke S, Klemme S (2006) Trace element partitioning between apatite and silicate melts. Geochim Cosmochim Acta 70:4513–4527

Putnis A (2009) Mineral replacement reactions. In: Oelkers EH, Schott J. (Eds), Thermodynamics and kinetics of water–rock interaction. Rev Mineral Geochem 30:87–124

Rasmussen CMØ, Ullmann CV, Jakobsen KG, Lindskog A, Hansen J, Hansen T, Eriksson ME, Dronov A, Frei R, Korte C, Nielsen AT, Harper DAT (2016) Onset of main Phanerozoic marine radiation sparked by emerging Mid Ordovician icehouse. Sci Rep 6:18884

Rivers T (2015) Tectonic setting and evolution of the Grenville Orogen: an assessment of progress over the last 40 years. Geosci Can 42:77–124

Schmieder M, Tohver E, Jourdan F, Denyszyn SW, Haines PW (2015) Zircons from the Acraman impact melt rock (South Australia): shock metamorphism, U–Pb and $^{40}Ar/^{39}Ar$ systematics, and implications for the isotopic dating of impact events. Geochim Cosmochim Acta 161:71–100

Schmieder M, Shaulis BJ, Lapen TJ, Buchner E, Kring DA (2019) In situ U-Pb analysis of shocked zircon from the Charlevoix impact structure, Québec, Canada. Meteorit Planet Sci 54:1808–1827

Schmitz B (2013) Extraterrestrial spinels and the astronomical perspective on earths geological record and evolution of life. Geochem 73:49–53

Schmitz B, Farley KA, Goderis S, Heck PR, Bergström SM, Boschi S, Claeys P, Debaille V, Dronov A, Van Ginneken M, Harper DA (2019) An extraterrestrial trigger for the mid-Ordovician ice age: dust from the breakup of the L-chondrite parent body. Science Advances 5:1–10

Schmitz B, Harper DT, Peucker-Ehrenbrink B, Stouge S, Alwmark C, Cronholm A, Bergström SM, Tassinari M, Xiaofeng W (2008) Asteroid breakup linked to the Great Ordovician biodiversification event. Nat Geosci 1:49–53

Scoates JS, Chamberlain KR (2002) Geochronolic, geochemical and isotopic constrains on the origin of monzonitic and related rocks in the Laramie anorthosite complex, Wyoming, USA. Precam Res 124:269–304

Seifert W, Thomas R, Rhede D, Förster HJ (2010) Origin of coexisting wüstite, Mg-Fe and REE phosphate minerals in graphite-bearing fluorapatite from the Rumburk granite. Euro J Mineral 22:495–507

Servais T, Harper DAT (2018) The Great Ordovician Biodiversification Event (GOBE): definition, concept and duration. Lethaia 51:151–164

Shafiqullah M, Tupper WM, Cole TJS (1968) K-Ar ages on rocks from the crater at Brent, Ontario. Earth Planet Sci Lett 5:148–152

Sláma J, Košler J, Condon DJ, Crowley JL, Gerdes A, Hanchar JM, Horstwood MSA, Morris GA, Nasdala L, Norberg N, Schaltegger U, Schoene B, Tubrett MN, Whitehouse MJ (2008) Plešovice zircon—a new natural reference material for U-Pb and Hf isotopic microanalysis. Chem Geol 249:1–35

Spear FS, Pyle JM (2000) Apatite, monazite, and xenotime in metamorphic rocks. Rev Mineral Geochem 48:293–335

Stacey JS, Kramers JD (1975) Approximation of terrestrial lead isotope evolution by two-stage model. Earth Planet Sci Lett 26:207–221

Steiger RH, Jäger E (1977) Submission on Geochronology: convention on the use of decay constants in geo- and cosmochronology. Earth Planet Sci Lett 36:359–362

Thomson SN, Gehrels GE, Ruiz J (2012) Routine low-damage apatite U-Pb dating using laser ablation-multicollector-ICPMS. Geochem Geophys Geosyst 13:1–23

Timms NE, Erickson TM, Pearce MA, Cavosie AJ, Schmieder M, Tohver E, Reddy SM, Zanetti MR, Nemchin AA, Wittmann A (2017) A pressure–temperature phase diagram for zircon at extreme conditions. Earth Sci Rev 165:185–202

Trotter JA, Williams IS, Barnes CR, Lécuyer C, Nicoll RS (2008) Did cooling oceans trigger Ordovician biodiversification? Evidence from conodont thermometry. Science 321:550–554

Walton EL, Hughes A, MacLagan EA, Herd CDK, Dence MR (2017) A previously unrecognized high-temperature impactite from the Steen River impact structure, Alberta, Canada. Geology 45:291–294

Walton EL, Timms NE, Hauck TE, MacLagan EA, Herd CDK (2019) Evidence of impact melting and post-impact decomposition of sedimentary target rocks from the Steen River impact structure, Alberta, Canada. Earth Planet Sci Lett 515:173–186

Watson EB, Green TH (1981) Apatite/liquid partition coefficients for rare earth elements and strontium. Earth Plan Sci Lett 56:405–421

Webby BD, Paris F, Droser ML, Percival IC (2004) The Great Ordovician Biodiversification Event. Columbia University Press, New York, NY, p 496

Wittmann A, Kenkmann T, Schmitt RT, Stöffler D (2006) Shock-metamorphosed zircon in terrestrial impact craters. Meteorit Planet Sci 454:433–454

Zappala V, Cellino A, Gladman BJ, Manley S, Migliorini F (1998) Asteroid showers on Earth after family breakup events. Icarus 134:176–179